The effect of mass loading and inter-particle collisions on the development of the polydispersed two-phase flow downstream of a confined bluff body

By J. BORÉE[1]†, T. ISHIMA[2] AND I. FLOUR[3]

[1]Institut de Mécanique des Fluides, UMR CNRS/INPT-UPS 5502
Allée du Professeur Camille Soula, 31400 Toulouse, France
[2]Gunma University, Tenjin, Kiryu 376-8515, Japan
[3]EDF – R&D, 6, Quai Watier, 78400 Chatou, France

The effect of mass loading and inter-particle collisions on the development of the polydispersed two-phase flow downstream of a confined bluff body is discussed. The bluff-body flow configuration, which is one of the simplest turbulent recirculating flows, is relevant for applications and forms the basis of numerous combustion devices. The present data are obtained for isothermal conditions by using a two-component phase-Doppler anemometer allowing size and velocity measurements. Polydispersed glass beads are introduced into the flow. The statistical properties of narrow particle size classes are displayed and analysed in order to allow for the wide range of particle relaxation times. The evolution of mass fluxes and mass concentration per size class is estimated from the PDA data. A correction is introduced to ensure that the mass flow rate of particles per size class from data integration is correct.

We show that the development of the continuous phase is very sensitive to initial mass loading of the inner jet. An increase in mass loading corresponds to an increase in momentum flux ratio between the central jet and annular flow. In the present situation, this implies a complete reorganization of the recirculation zone and the turbulent field. The importance of direct modulation of turbulence induced by particles is demonstrated in the inner jet. Moreover, our data confirm that the prediction of fluid/particle velocity correlation is essential to take these effects into account for partly responsive beads.

We show that the sensitivity to mass loading greatly affects the dispersion of the glass beads. Particles recirculate at the lowest mass loading and the mass concentration of the dispersed phase in the recirculation zone and in the external shear layer is high. On the other hand, the memory of the initial jet is detected far downstream at the highest loading and the dispersion of particles is reduced. Axial or radial profiles of mean and r.m.s. velocity of the dispersed phase are displayed and analysed. The role of large-scale intermittency is discussed. Relevant Stokes numbers are introduced to account for different driving mechanisms in the turbulent field. Non-Stokesian effects are particularly important. We show that the anisotropy of the particle fluctuating motion is large and associated with production mechanisms via interaction with mean particle velocity gradients. A focus on the jet stagnation region proves that the particulate flow is very sensitive to inertia effects and that no local equilibrium with the fluid turbulence can be assumed when modelling such a configuration.

† Present address: LEA–ENSMA, Teleport 2, BP 109, 86960 Futuroscope Cedex, France.

Finally, even at the small volume ratio considered here, we prove that it is highly probable that inter-particle collisions occur in the jet stagnation region at low mass loading and all along the inner jet flow at the highest mass loading. Redistribution of mean momentum and fluctuating kinetic energy between all colliding classes is therefore expected, which implies a fully coupled fluid and particle system.

The data and analysis presented provide a severe test case for the recent development in two-phase flow modelling and offer further challenges both to experimentation and model development. The validated data set has been selected for benchmarking and is available on the internet.

1. Introduction

Turbulent concentric jet flows separated by a bluff body form the basis of numerous combustion devices referred to as bluff body stabilized flames (Scheffer, Kelly & Namazian 1987). The recirculating flow geometry implies high turbulence levels and mixing rate, which result in the stabilization of the flame. The flame is significantly shorter than jet flames and the level of pollutant emissions is reduced. Although these types of flow are one of the simplest turbulent recirculating flows, they present severe challenges to computational models. This combined relevance for practical combustion devices and fundamental understanding of turbulence and mixing has driven a considerable amount of experimental and computational research work in single-phase isothermal and combustion conditions. The importance of large scale structures and flow intermittency has been emphasized particularly by flow visualization (Chin & Tankin 1992), by conditional velocity measurements (Scheffer *et al.* 1987, 1994) and by instantaneous concentration determination using imaging techniques (Namazian, Kelly & Scheffer 1992).

An experimental study of a two-phase bluff-body flow laden with dense solid particles is presented in this paper. This work is motivated by the practical importance of two-phase combustion in a wide range of applications including propulsion, energy conversion and industrial processes. In most applications, the dispersed phase is introduced in a recirculating geometry in which recirculation is induced by a solid body or by swirl generated at the air inlet. The dispersed phase can be solid particles, e.g. coal particles (Abbas, Costen & Lockwood 1991) or liquid hydrocarbon droplets (Hardalupas, Liu & Whitelaw 1994). The residence time of the particles in the recirculation zone of high-temperature combustion products favours vaporization of liquid fuel (or devolatilization of coal products) and mixing. The behaviour of the particles in such flows, therefore, largely influences the stabilization of the flame, the rate of heat release, and the level of pollutant emissions.

Before studying these complex situations involving mass transfer and chemical reactions, we focus in the present work on the dispersion of spherical dense beads in isothermal conditions. Indeed, the interactions between small, partly responsive particles and turbulent flows imply many interdependent effects, many of which remain poorly understood. The development of good engineering models using either Eulerian (Elgobashi & Abou-Arab 1983; Simonin 1991; Vit, Flour & Simonin 1999) or Lagrangian (Berlemont, Desjonqueres & Gouesbet 1990; Sommerfeld 1993; Sommerfeld 1999) approaches is therefore particularly challenging.

The number of parameters in two-phase flows is very large. We will restrict ourselves to particles much heavier than the fluid and much smaller than the energetic

lengthscales of the turbulent flow. Well-qualified experiments and computations have been obtained in the sort of basic flows required by model developers. We can mention homogeneous and isotropic turbulence (Snyder & Lumley 1971; Wells & Stock 1983; Squire & Eaton 1990; Boivin, Simonin & Squire 1998); homogeneous sheared turbulence (Simonin, Deutch & Boivin 1995); channel and tube flows (Tsuji, Morikawa & Shiomi 1984; Kulick, Fessler & Eaton 1994; Wang & Squire 1996); boundary-layer flows (Rogers & Eaton 1991), simple free shear flows as shear layers (Hishida, Ando & Maeda 1992; Ishima, Hishada & Maeda 1993) and jets (Modaress, Tan & Elgobashi 1984; Hardalupas, Taylor & Whitelaw 1989; Prévost *et al.* 1996).

Particle inertia and particle mass loading are crucial parameters. The role of particle inertia is quantified by comparing an aerodynamic response time with the fluid timescale seen by the particles along their trajectories. The ratio of these timescales is defined as the particle Stokes number. A wide range of Stokes number is usually present at the same time if the size distribution is large. Studies have shown that both dispersion and instantaneous distribution of particles in the flow (Fessler, Kulick & Eaton 1994) strongly depend on the Stokes number. As statistical modelling is involved, the challenge is therefore to predict accurately the fluid statistics seen by the particles and the associated fluid/particle velocity correlations (Simonin 1991). These statistics are controlling the mean and turbulent momentum exchange rate between the phases. Their predictions provide a clear understanding, for example, of the large anisotropy of the dispersed phase turbulence observed in shear flows (Simonin *et al.* 1995; Fevrier & Simonin 1998).

An increase in mass loading results in a two-way coupling situation when the momentum exchange between particles and fluid results in a significant modulation of the base flow (Crowe 2000). The picture of turbulence modification by particles is, however, extremely complex and involves direct and indirect mechanisms. Reference experimental data for unchanged mean flow statistics (see e.g. Fessler & Eaton 1999) and important databases obtained by direct numerical simulations of forced homogeneous and isotropic turbulence (Squire & Eaton 1990; Boivin *et al.* 1998) have been analysed to study the direct effects. The numerical studies show particularly clearly that particles interfere with the dynamical processes of the turbulence itself. A non-uniform distortion of the spectra is observed with a relative increase of small-scale energy. Such distortion is also observed for small particles in the experimental works of Tsuji *et al.* (1984), Rogers & Eaton (1991) and Kulick *et al.* (1994). Note that, at a given mass loading, for small particles of given Stokes number, the particle Reynolds number is also identified as an important independent parameter in the experimental study of Fessler & Eaton (1999).

In inhomogeneous flows of non-uniform particle mass loading, large indirect changes occur through modifications of the mean fluid flow and turbulence production mechanisms via interaction with mean gradients. Moreover, the turbulent diffusion terms should also be changed. Unfortunately, no measurements of the turbulent diffusion terms in an inhomogeneous-particle-laden gas flow are yet available. Modulation of turbulence by particles, therefore, involves simultaneously complex mechanisms, and no satisfactory physical models can be found at the present time to deal with these phenomena (Squire & Eaton 1994).

Flow separation and large-scale structures are typical features of the bluff-body flow presented in this paper. The particles are released in the central jet flow only (figure 1). Moreover, the characteristics of the single-phase flow were carefully selected in order to obtain a distinct mean jet stagnation point on the axis of the recirculation zone. At moderate mass loading M_j (M_j is the ratio of the mass flux of particles to
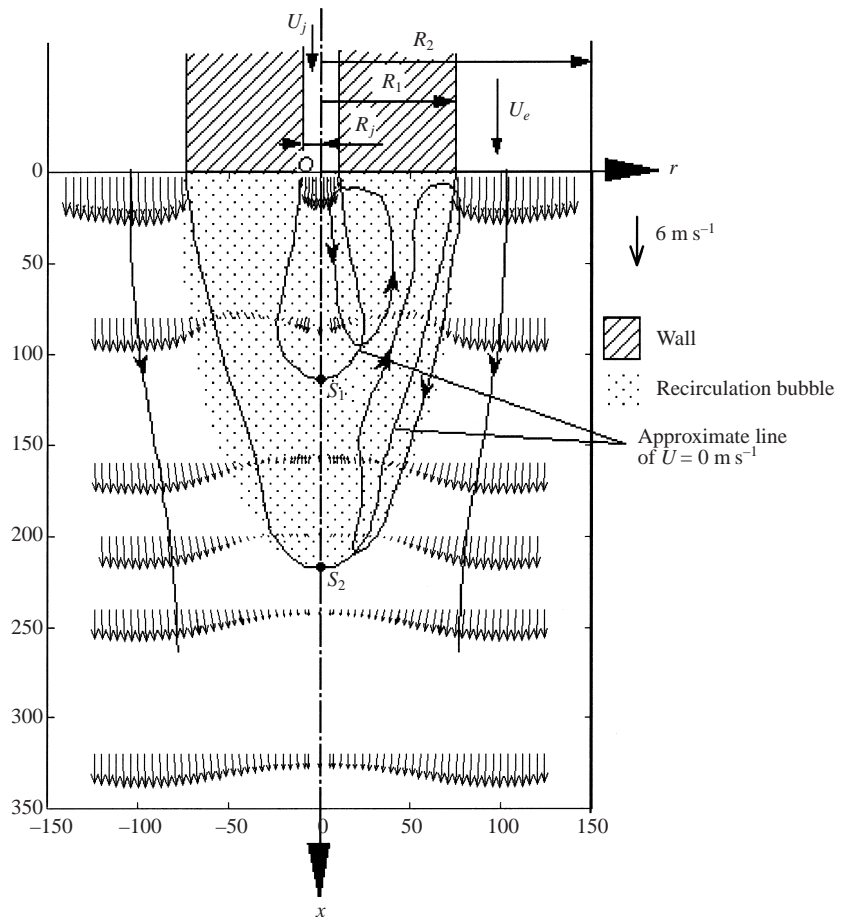
FIGURE 1. Geometry of the confined bluff body and measured mean velocity field in
single phase configuration.

the mass flux of air in the central jet flow), one objective of this study is, therefore, to investigate particle motion in the fluid stagnation region where the role of the inertia of the particles should be emphasized. This configuration is an additional contribution to the classical reference situations mentioned above. Note that particle motion in the stagnation zone of an impinging air jet was studied by Anderson & Longmire (1995). The physical situation is, however, completely different over a solid surface. Our data were made available for model testing. The complete data set, including accurate boundary conditions, at moderate mass loading $M_j = 22\%$ has been selected for benchmarking at the 'Ninth workshop on two-phase flow predictions' and can be obtained at the web site of the congress (Ishima *et al.* 1999).

The extreme sensitivity of the bluff-body flow to the value of the ratio of the momentum flux of the inner jet to the momentum flux of the annular jet is well known in single-phase situations (see e.g. Chen *et al.* 1990). In the presence of glass beads, the value of the mass loading M_j provides information about the proportion of the momentum flow rate carried by the particles to that carried by the gaseous phase in the inner jet. The development of the jet in the recirculation region and the dispersion of the particulate phase are thus expected to vary strongly with mass loading. A

second objective of this paper is, therefore, to provide and analyse experimental data at a higher mass loading $M_j = 110\%$. We will observe very important changes concerning both continuous and dispersed phases. These observations are believed to be of interest to test the recent developments in two-phase flow modelling because the results obtained numerically will indeed be very sensitive to the accurate description of the physical processes involved. We may wonder, in particular, if the direct modulation of turbulence by particles is important and has to be taken into account in engineering models. We will answer this question by comparing production via mean gradients with direct attenuation.

As far as the dispersed phase is concerned, the mean and fluctuating characteristics of most classes of the polydispersion are coupled at high mass loadings if particles exchange momentum with one another. To consider this important aspect, we will analyse the probability of particle/particle collisions by applying recent results of kinetic theory to binary mixtures of particles (Gourdel, Simonin & Brunier 1999). The volume ratio considered here is everywhere lower than 10^{-3}. Nevertheless, we will show that that collisions are very probable in the highly turbulent jet region. The effects expected for the present complex flow are discussed in §5.

2. Experimental set-up; measurement techniques

2.1. *Geometry of the test facility*

The geometry of the confined bluff body is given in figure 1. The data were obtained in a flow-loop of EDF – R&D. The experiment has been performed in the vertical axisymmetric airflow downstream of the bluff body. The length of the measurement section is $L = 1500$ mm. The sketch of the overall flow development drawn here was derived from systematic axial and lateral mean velocity profiles in single phase configuration.

The outer and inner radiuses of the annular outer region are, respectively, $R_2 = 150$ mm and $R_1 = 75$ mm. The blockage ratio ($BR = R_1^2/R_2^2 = 25\%$) of this bluff-body flow is low. Effects of confinements on the development of the recirculation zone should be moderate and have been studied by Perrin *et al.* (1990). The external volume flux is kept constant at $Q_e = 780 \, \mathrm{m}^3 \, \mathrm{h}^{-1}$. The mean (maximum) velocity of the annular flow is $\overline{U_e} = 4.1 \, \mathrm{m \, s}^{-1}$ (max $(U_e) = 6 \, \mathrm{m \, s}^{-1}$) and the Reynolds number of the flow is $Re \approx 20\,000$. This relatively low value of the external velocity was chosen in order to use a reasonable external volume flux and to overcome seeding problems. The length of the straight annular section upstream of the test section is $L_e = 2$ m. With $2L_e/(R_2 - R_1) \approx 54$, the turbulent boundary layer can be considered as established, but the turbulent annular flow is suspected to be under slight development (Comte-Bellot 1965). The inner tube jet ($R_j = 10$ mm; $U_j(r = 0) = 4 \, \mathrm{m \, s}^{-1}$) is generated by compressed air flows on the axis of the recirculation, as shown in figure 1. The tube flow is established with $2L_e/D_j = 200$. The volume flux of the jet is $Q_j = 3.4 \, \mathrm{m}^3 \, \mathrm{h}^{-1}$ and the ratio of the jet volume flux to the annular flow volume flux is very low (0.5%). This corresponds to a mean velocity $\overline{U_j} = 3.4 \, \mathrm{m \, s}^{-1}$. These characteristics were chosen in order to obtain a single-phase flow with stagnation points in the recirculation. This particular regime of the bluff-body flow is often referred to as 'external air flow dominated' in the literature (Scheffer *et al.* 1994).

2.2. *Glass particles*

Glass particles are released in the conducting pipe of the inner jet by a particle feeder. All parts of the set-up were carefully earthed and the air flow is slightly humid

D (µm)	20	30	40	50	60	70	80	90	100
Mass distribution	0.004	0.005	0.091	0.224	0.264	0.215	0.107	0.065	0.025
Number distribution	0.085	0.028	0.234	0.295	0.202	0.103	0.034	0.015	0.004

TABLE 1. Initial distribution of the particle size.

in order to suppress the influence of static electricity. The material density of the glass particle is $\rho_p = 2470\,\text{kg m}^{-3}$. All flow conditions and particle mass loadings are monitored on a workstation. The mass loading is controlled accurately in a closed loop by weighting the particle feeder continuously. Two mass flow rates of particles of $1\,\text{kg h}^{-1}$ and $5\,\text{kg h}^{-1}$ corresponding to contrasted inner jet mass loading ratio of $M_j = 22\%$ and $M_j = 110\%$, respectively, have been selected. Note that the mass loading ratio of the global flow is in each case very weak: $M_t = 0.1\%$ and $M_t = 0.5\%$, respectively.

The particles were new at the beginning of this work. The initial distribution of the size of the spherical glass beads is displayed in table 1. The size classes are divided into 15–25 µm, 25–35 µm, ... 95–105 µm. The initial particle size distribution covers a wide range of size classes from 20 µm to 100 µm. The corresponding mass averaged diameter of the distribution is $\overline{d_{pM}} = 63$ µm. The number frequency distribution was deduced from the mass frequency distribution. The corresponding number averaged diameter of the distribution is $\overline{d_{pN}} = 50$ µm. The distribution was checked several times during the acquisition of the database in order to check for possible breaking of particles during runs. No noticeable differences were detected. Moreover, visual inspection with a microscope revealed very few non-spherical glass fragments.

The Stokes number of a particle size class is defined as the ratio of the particle aerodynamic time constant τ_p to an appropriate turbulent timescale τ_j. The Stokesian particle relaxation time for $\rho_p \gg \rho_f$ is $\tau_{pST} = \rho_p d_p^2 / 18\mu$ where d_p is the median diameter of the particle size class, ρ_p is the particle density and μ is the fluid viscosity. This characteristic time calculation is interesting as a first order of magnitude for particle Reynolds numbers up to order of unity. τ_{pST} varies significantly: for size classes 20, 60 and 100 µm, its value is, respectively, $\tau_{pST} = 3, 27$ and 76 ms. However, we will see that the assumption of Stokes flow around an isolated particle is not satisfied for many cases in our experimental conditions. Appropriate corrections will be taken into account.

2.3. *PDA settings*

Particular care was taken to seed both outer and inner single-phase flows with approximately the same volumetric concentration of tracers. Four water injectors designed for spreading water mist as tracer particles are located 2 m upstream of the measurement region and are used to seed the annular flow. Many seeding techniques were tested to find a suitable method for this experiment. Because of the difficulty in obtaining enough volume flux of the seeding particles, and for the safety of experiments, water droplets were chosen. No building up of particles is detected in the stagnation and early wake region of interest. Moreover, visual inspection and measurements with and without water droplets revealed no detectable effects on the behaviour of the particulate phase even at high mass loading when large particles are expected to collide with each other. In particular, no changes in the particle size distribution were observed with or without the water mist in the preparative

experiment. Smoke tracers generated by a smoke machine are added to the central jet flow.

For making measurements with a laser-Doppler system in an axisymmetric geometry, 15 optical windows consisting of thin plastics sheets with a thickness of 0.3 mm are located along the test section. A two-component phase Doppler anemometer produced by Dantec (Particle Dynamics Analyser: PDA) is used. For accuracy and the convenience of the displacement, an optical fibre system is preferred. The total inter section angle of the incident beam is 1.5°. The receiving optics is settled at a 64° off-axis angle from the incident beam to minimize the contribution of the reflected light. A description of the parameters of the system is given in Appendix A. The optical windows are on the incident beam side only. The actual off-axis angle is therefore slightly changed from the 64° at the outer side of the measuring range because of the refraction effect on the cylindrical wall of the test section. The off-axis angle error was checked and is not significant for diameter measurements.

The refractive index used is set as 1.51 and corresponds to a normal glass particle. In this experiment, water droplets and smoke were used as the tracer particles. Their refractive indexes are not equal to that of a glass particle. However, the result from the single-phase flow measurements with only seeding particles but performed with the refractive index of the glass particle indicates that the mean diameter of the water droplets is less than 5 μm and that of smoke is 2 μm. In addition, the results from two-phase flow without tracers show that very few glass particles of less than 10 μm diameter exist in the experimental region. Therefore, all the particles of less than 5 μm diameter are treated as tracer particles. We have verified that all the particles in this size-class can be considered as good tracers of the continuous phase. Measurements are carried out for the continuous and dispersed phases simultaneously. Unless specified, we perform statistical averaging of at least a thousand independent samples in each size-class. Consequently, estimated statistical absolute errors for mean values and relative errors for standard deviation values are, respectively, $\Delta U \approx 0.06u'$ and $E_\sigma \approx 5\%$ with a 95% confidence level.

The flow will be described using a cylindrical coordinate system (x, r, θ) to indicate the axial (downward), radial and azimuthal directions. The origin is set on the edge of the bluff body and at the centre of the inner jet (figure 1). The components of the instantaneous velocity field are denoted, respectively, by (U, V, W) where V is the radial component and W is the azimuthal component. No mean swirling motion was detected to within our measurement precision. Subscripts f and p indicate, respectively, fluid and particle properties. The symbols $\langle \ \rangle_f$ and $\langle \ \rangle_p$ indicate averaging operators associated, respectively, to fluid and particle phases. Subscript $\langle \ \rangle_{pi}$ is used when the particular size class number i is analysed. The components of the instantaneous fluctuating velocity field are denoted, respectively, by (u, v, w). The u' and v' stand, respectively, for longitudinal and radial standard deviation.

2.4. *Computation of mass fluxes and mass concentration*

The mass and number fluxes and mass and number concentrations are very important data. However, no reliable direct measurement of these quantities is possible with PDA. The intensity of the light in the measurement volume is Gaussian. The measurement volume seen by large particles is therefore larger than the one seen by small particles. This induces a systematic bias if no care is taken. Moreover, the amount of rejected data is not known and eventually varies with the size class. Sommerfeld & Qiu (1995) have proposed a method in which the maximum amplitude of the Doppler burst and the integral of the energy of the burst above a given threshold have to be
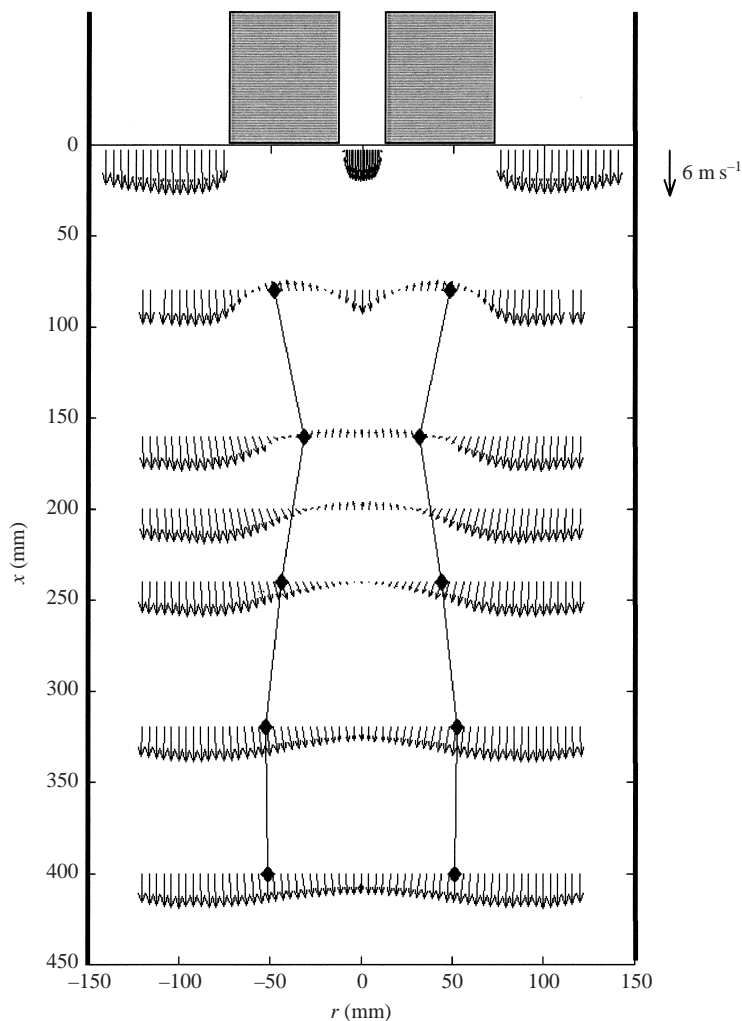
FIGURE 2. Vector plot of the mean gas flow at $M_j = 22\%$. ◆, mean distance from axis (equation (3.1)) for 60 μm particle size class.

registered by PDA. This is impossible when commercial systems are used. A method is proposed in Appendix B where the local mass flux is corrected independently for each size class for varying size of the measurement surface seen by the receiving optics and for rejected data. By 'corrected local mass flux', we mean that the mass flow rate of particles per size class obtained by integration from the data is correct. This is one advantage of confined flow configurations, and measurements discussed in this work show that the assumptions made in Appendix B provide a good evaluation.

3. Development of the polydispersed flow field at moderate mass loading

In this section, we present and discuss the downstream evolution of the air and particulate flow fields at a moderate mass loading ($M_j = 22\%$). A vector plot of the overall flow development is presented in figure 2. In the same figure, we have plotted the longitudinal evolution of the mean distance from the axis for the 60 μm particle
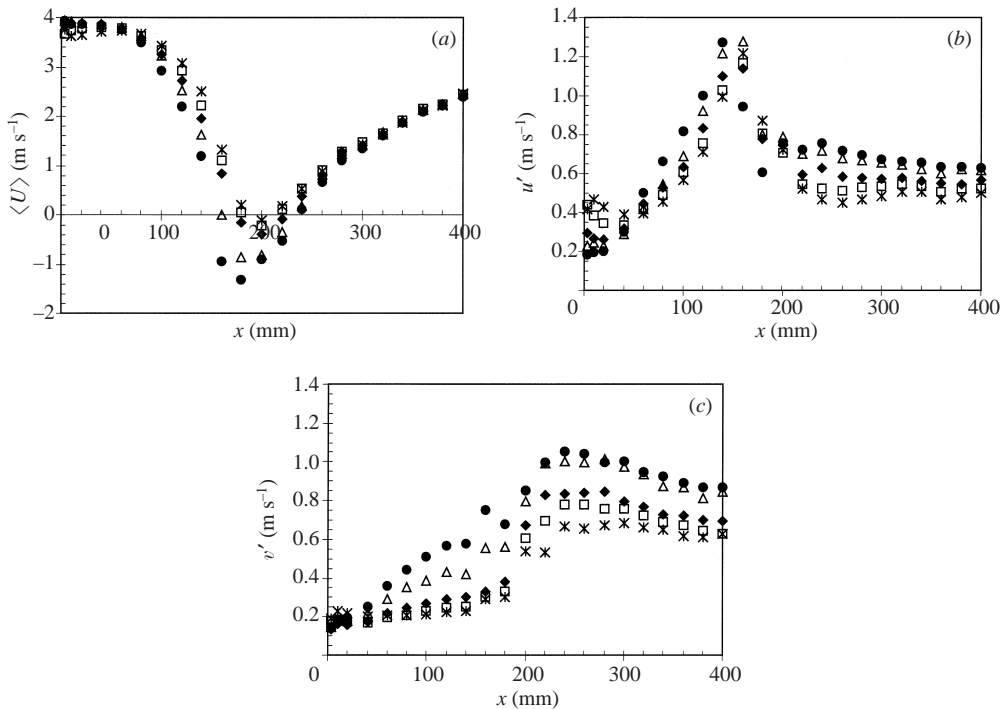
FIGURE 3. Axial evolution of the mean and r.m.s. velocity of continuous and dispersed phase at $M_j = 22\%$ ●, tracers; △, $d_p = 20\,\mu\text{m}$; ◆, $d_p = 40\,\mu\text{m}$; □, $d_p = 60\,\mu\text{m}$; ✳, $d_p = 80\,\mu\text{m}$. (*a*) mean longitudinal velocity; (*b*) r.m.s. longitudinal velocity; (*c*) r.m.s. radial velocity.

class (see equation (3.1)). To provide more quantitative information, figure 3 compares the axial evolution of the mean axial velocity, r.m.s. axial velocity and r.m.s. radial velocity for air and for size classes 20, 40, 60 and 80 μm. Radial profiles of mean axial and radial velocities, r.m.s. axial and radial velocities and Reynolds shear stress at $x = 3$, 80, 160 and 240 mm are presented in figures 4–8. Radial profiles of mean mass flux and mean mass concentration of the 60 μm class are presented respectively in figures 9 and 10.

3.1. *Flow field of the continuous phase*

The carrying air flow field can be schematically decomposed into different regions.

A jet develops at the exit of the central tube (figure 2). This jet is surrounded by a recirculation upward flow which 'feeds' both the initial entrainment in the jet and the annular shear layer developing at the edge of the bluff body. The central region at $x = 80$ mm corresponds to this jet region (figures 4–8). The production of axial r.m.s. velocity is clearly dominant. Noticeably, the radial r.m.s. velocity, approximately constant in the recirculating region, is much lower in the core of the jet (figure 7).

The central jet flow is stopped rapidly in the recirculating flow. In the following, S_1 denotes the mean stagnation point of the jet. The high turbulent shear stress and the axial pressure gradient created by the reverse flowing air are the main contributors to the rapid decrease of the mean longitudinal velocity (figure 3*a*). The turbulent timescale associated with the longitudinal velocity decrease and related phenomena near S_1 is $\tau_{dec} = (\partial\langle U_f\rangle_f/\partial x)^{-1}$. It will be shown in §4 that τ_{dec} depends strongly on the ratio of the momentum flux of the inner jet to the momentum flux of the outer annular flow. τ_{dec} is small at $M_j = 22\%$ with $\tau_{dec} = 15$ ms. The evolution of the axial
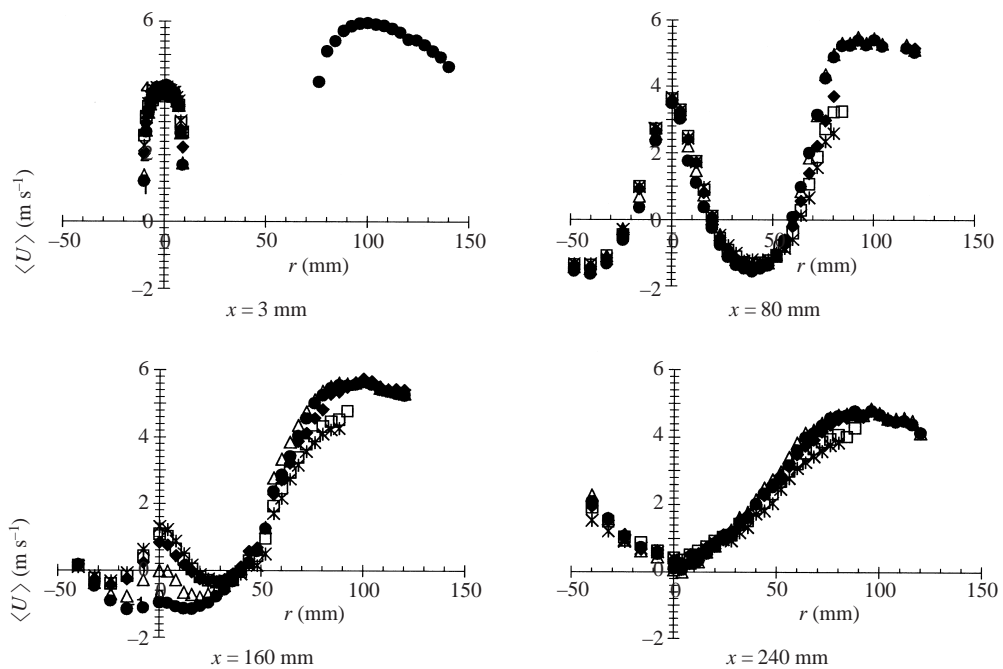
FIGURE 4. Radial profiles of mean longitudinal velocity of the two-phase flow at $M_j = 22\%$.
●, tracers; △, $d_p = 20\,\mu\text{m}$; ◆, $d_p = 40\,\mu\text{m}$; □, $d_p = 60\,\mu\text{m}$; ✻, $d_p = 80\,\mu\text{m}$
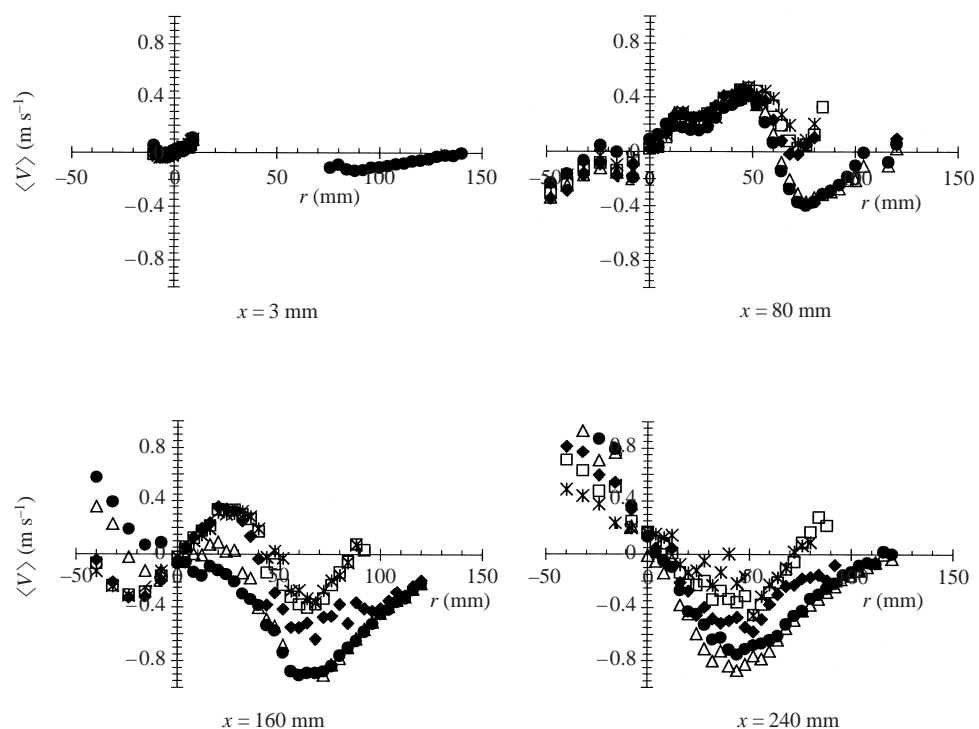

FIGURE 5. Radial profiles of mean radial velocity of the two-phase flow at $M_j = 22\%$. ●, tracers;
△, $d_p = 20\,\mu\text{m}$; ◆, $d_p = 40\,\mu\text{m}$; □, $d_p = 60\,\mu\text{m}$; ✻, $d_p = 80\,\mu\text{m}$.
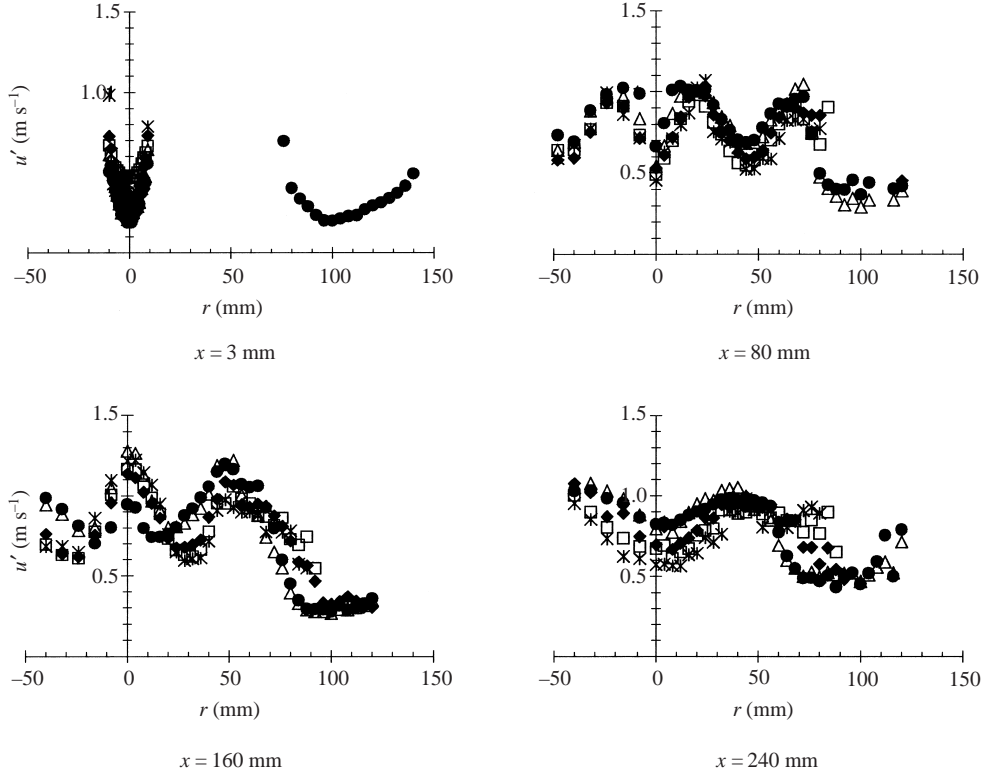
FIGURE 6. Radial profiles of fluctuating longitudinal velocity of the two-phase flow at $M_j = 22\%$. ●, tracers; △, $d_p = 20\,\mu\text{m}$; ◆, $d_p = 40\,\mu\text{m}$; □, $d_p = 60\,\mu\text{m}$; ✳, $d_p = 80\,\mu\text{m}$.

velocity fluctuations in the jet stagnation region displayed in figures 3(*b*) and 6 is typical for bluff-body flows (Scheffer *et al.* 1994). A clear maximum of u'_f is detected and the corresponding anisotropy on the axis is high with $u'_f/v'_f \approx 2.2$. The location of this maximum corresponds to the first mean stagnation point. At this location, the flows are opposed along the axis. Turbulence is therefore submitted to an axial compression and a radial strain and the production of axial velocity fluctuations $P_{u'_f} = -2\langle u_f u_f \rangle_f \partial \langle U_f \rangle_f / \partial x$ is important.

The negative values of $\langle U_f \rangle_f$ at $x = 80$ and $160\,\text{mm}$ indicate the location and radial extent of the recirculation zone. The mean radial velocity $\langle V_f \rangle_f$ shows inward flow (negative values) that converges toward the centreline. The fluid timescale chosen to characterize a large-eddy motion in the recirculating region (figure 2) and in the early wake developing downstream can be based on an approximate large-eddy property $\tau_{rec} = 4R_1/U_e$ (Hardalupas, Taylor & Whitelaw 1992; Fessler & Eaton 1999) where R_1 is the radius of the bluff body, U_e is the maximum external velocity and $U_e/4 = 1.5\,\text{m s}^{-1}$ is an order of magnitude of the maximum mean upstream velocity measured in the recirculating region. τ_{rec} is much larger than τ_{dec} with $\tau_{rec} \approx 50\,\text{ms}$. Most particles are therefore responsive to the recirculation.

The effect of shear production in the external annular shear layer is evidenced on the radial evolutions of axial fluctuating velocities (figure 6). Note that contrary to what is observed in quasi-parallel shear flows, a significant maximum of production of v'_f is measured at the radial edge of the recirculation zone. This maximum corresponds
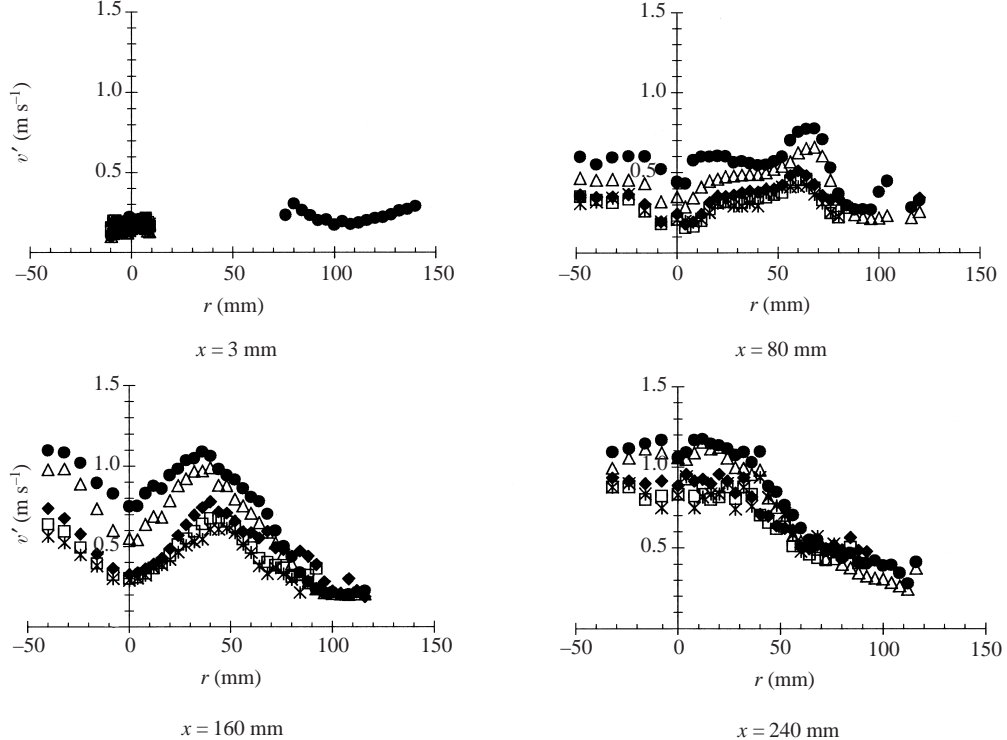
FIGURE 7. Radial profiles of fluctuating radial velocity of the two-phase flow at $M_j = 22\%$.
●, tracers; △, $d_p = 20\,\mu\text{m}$; ◆, $d_p = 40\,\mu\text{m}$; □, $d_p = 60\,\mu\text{m}$; ✳ $d_p = 80\,\mu\text{m}$.

to the maximum value of $(\partial V_f/\partial r)$ (Ishima *et al.* 2000) and to the peak value of v'_f (figure 7).

A second mean stagnation point S_2 is located at approximately $x = 240\,\text{mm}$. A transition to a wake-like region is clearly seen. The end of the recirculating bubble is associated with a typical axial strain and radial compression. Figures 3(*c*) and 7 show that the radial fluctuating velocity on the axis is very high at this location. Qualitatively, this high level of v'_f has been shown to be associated with large-scale flow oscillations and bimodal radial velocity p.d.f. (Scheffer *et al.* 1987, 1994). Such radial velocity p.d.f.s were also observed in this work. Further downstream, in the early wake region, the radial fluctuations on the axis decrease, but remain greater than u'_f with $u'_f/v'_f(r = 0) \approx 0.7$.

3.2. *Dispersion of the glass beads*

The mass fluxes and mass concentration have been evaluated from the measurements for the different particle size classes. Equations (B.12) and (B.13) (see Appendix B) are used in this complex three-dimensional turbulent flow. A global measure is drawn in figure 2. The mean distance from the axis for a particle class i is defined classically by:

$$R_{pi} = \int_0^{R_2} rC_i 2\pi r\,\text{d}r \Big/ \int_0^{R_2} C_i 2\pi r\,\text{d}r. \tag{3.1}$$

C_i is the mean local number concentration for class i. Figure 2 has to be compared with figure 13 which shows a downstream evolution of R_{pi} clearly different at $M_j = 110\%$.
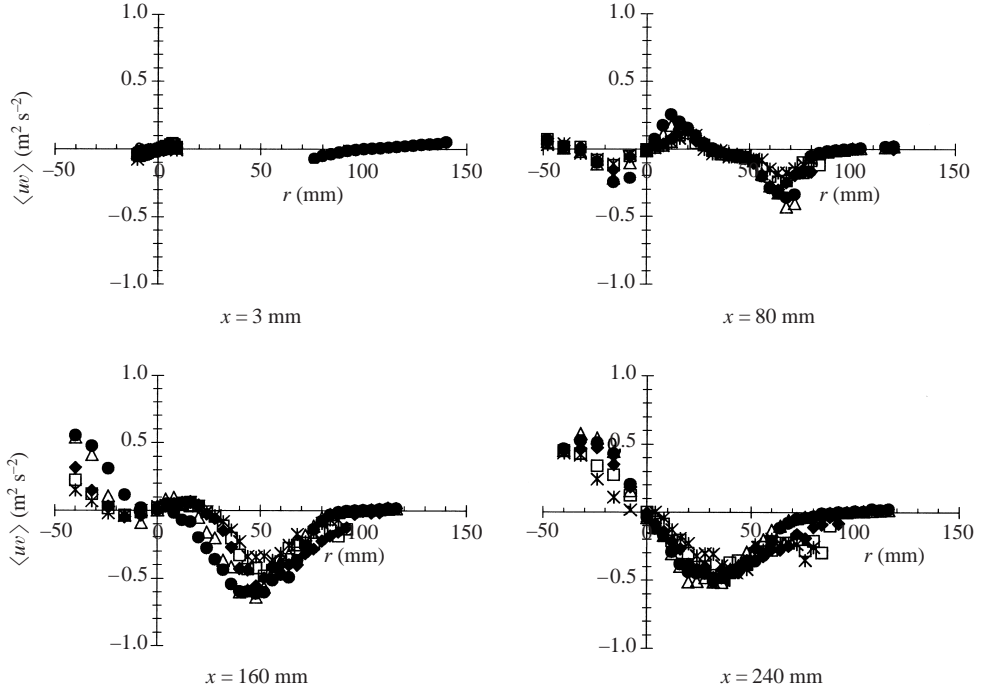
FIGURE 8. Radial profiles of Reynolds shear stress of the two-phase flow at $M_j = 22\%$. ●, tracers; △, $d_p = 20\,\mu m$; ◆, $d_p = 40\,\mu m$; □, $d_p = 60\,\mu m$; ✻ $d_p = 80\,\mu m$.
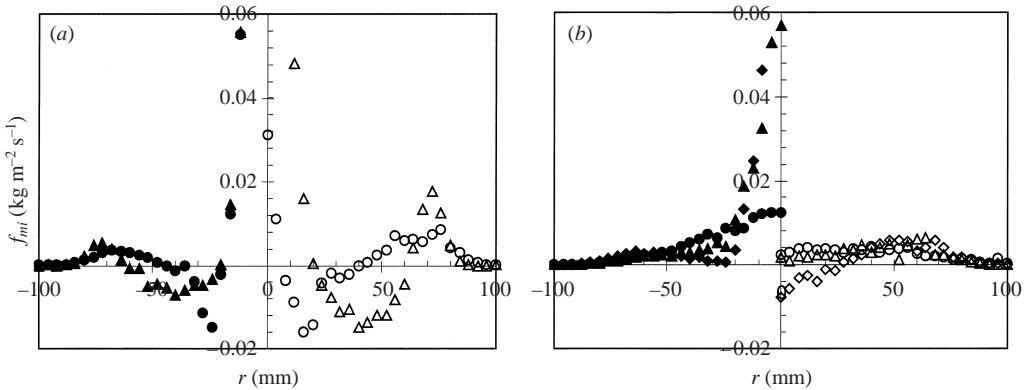

FIGURE 9. Radial profiles of mean longitudinal mass flux f_{mi} (right-hand side and open symbols: $M_j = 22\%$; left-hand side and filled symbols: $M_j = 110\%$ and $\frac{1}{5}f_{mi}$). (a) △ and ▲, $x = 80\,mm$; ○ and ●, $x = 160\,mm$, (b) ◇ and ◆, $x = 200\,mm$; △ and ▲, $x = 240\,mm$; ○ and ●, $x = 320\,mm$.

From figure 2, we guess that particles recirculate at $M_j = 22\%$ and are dispersed in the recirculating region. R_{p60} is minimum near S_1. We will show that the mean concentration of particles near the axis is high in this mean stagnation region. Particles are very efficiently dispersed downstream of S_1.

The radial profiles of mean longitudinal mass flux $f_{mi}^{(1)}$ and mean mass concentration C_{mi} are presented in figures 9 and 10, respectively. Data relative to the 60 μm size class only are presented for better clarity, and comments relative to the evolution of the local mass distribution of the polydispersion are made. The right-hand sides of
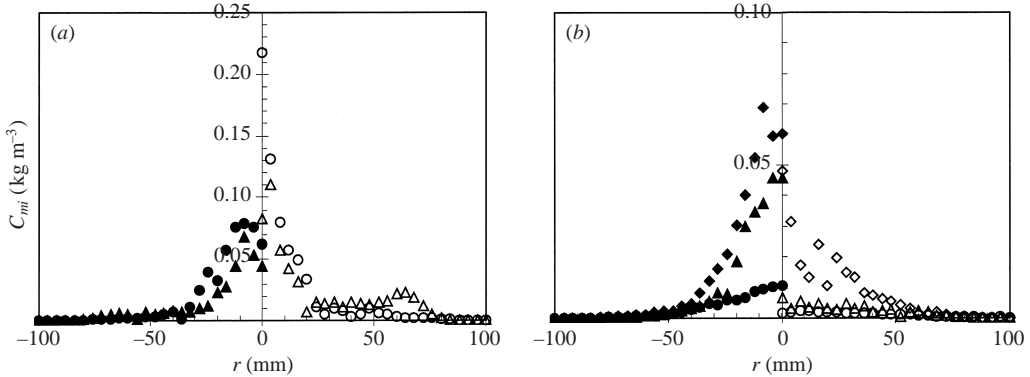
FIGURE 10. Radial profiles of mean mass concentration C_{mi} (right-hand side and open symbols: $M_j = 22\%$; left-hand side and filled symbols: $M_j = 110\%$ and $\frac{1}{5}C_{mi}$). (*a*) $*$, $x = 3$ mm; $\triangle$ and $\blacktriangle$, $x = 80$ mm; $\bigcirc$ and $\bullet$, $x = 160$ mm. (*b*) $\diamond$ and $\blacklozenge$, $x = 200$ mm; $\triangle$ and $\blacktriangle$, $x = 240$ mm; $\bigcirc$ and $\bullet$, $x = 320$ mm.

figures 9 and 10 correspond to $M_j = 22\%$ whereas the left-hand side corresponds to $M_j = 110\%$ and will be discussed in §4. We feel that it is important to present a direct comparison. Accordingly, the high mass loading values are divided by 5. Both sides, therefore, artificially correspond to the same initial mean mass flux and mean mass concentration.

The signature of the jet, recirculation region and outer shear layer is clear at the axial position $x = 80$ mm. The high value of $f_{mi60}^{(1)}$ on the axis is not reported in figure 9(*a*) in order to focus on the recirculating region. On the axis and at $x = 80$ mm, the longitudinal mass fluxes at $M_j = 22\%$ and 110% are $f_{mi60}^{(1)} = 0.29$ and 1.1 kg m^{-2} s^{-1}, respectively. The particles recirculate at the lowest mass loading; figure 9(*a*) shows that the relative mean longitudinal mass flux directed upstream in the recirculating region and downstream in the outer shear layer is much more intense in this situation. In figure 10(*a*), we see clearly that the mean mass concentration is approximately constant in the recirculating region at $x = 80$ mm and reaches a local maximum in the outer shear layer. This property is particularly important for flame stabilization in combustion situations (Hardalupas *et al.* 1994).

The station $x = 160$ mm is located slightly upstream of the mean stagnation point of 60 μm particles (figure 3*a*) at the lowest mass loading. In figure 9(*a*), we see that $f_{mi60}^{(1)}$ is small on the axis. Moreover, the local mean mass concentration of particles measured at this station is three time greater than the initial mean mass concentration on the axis for $M_j = 22\%$ (figure 10*a*). Such behaviour is natural near a stagnation point. Note that the broadening of the outer shear layer is also clear at $x = 160$ mm in figure 10(*a*). Finally, the internal dynamics of the recirculating bubble are responsible for an efficient radial dispersion of the glass beads. The profiles of $f_{mi60}^{(1)}$ and of C_{mi60} are indeed very flat all across the wake of the bluff body (right-hand side of figures 9*b* and 10*b*).

Such a discussion could be performed for other size classes. It would be a rather tedious presentation in the present context. Contrasted size classes, however, imply quantitatively a different behaviour that should have an important signature on the local mean mass distribution of the polydispersion. Such local mean mass frequency distributions are presented at representative locations on the axis in figure 11 at $M_j = 22\%$. These detailed results also show the coherence of the present database and data reduction techniques. A striking effect of axial particle injection is again detected
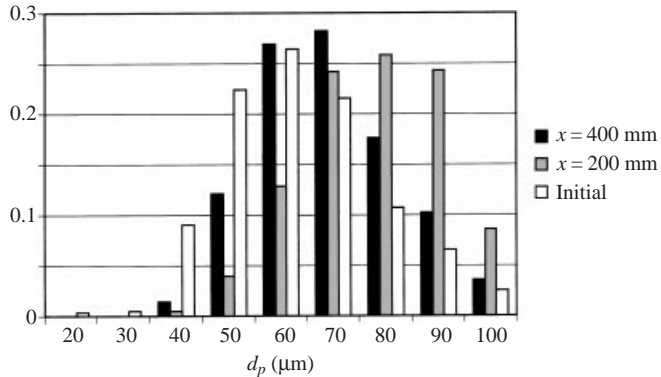
FIGURE 11. Local mean mass distribution on the axis $M_j = 22\%$.

at the lowest mass loading in figure 11. The location at $x = 200$ mm corresponds to a very low mean velocity of the large size classes in the recirculation zone and therefore to a high mean mass concentration for these classes. The mass frequency distribution is therefore strongly shifted toward large size classes and the mass averaged diameter of the polydispersion at $x = 200$ mm is $\overline{d_{pM}} = 78\,\mu$m. This value is 24% higher than the initial value $\overline{d_{pM}} = 63\,\mu$m. At the exit of the measurement domain ($x = 400$ mm) and at $M_j = 22\%$, the mass averaged diameter of the polydispersion on the axis is $\overline{d_{pM}} = 69\,\mu$m. This value is larger than the initial value because small size classes disperse more efficiently. Such observations show clearly that taking into account the polydispersed nature of the particles is necessary when modelling these flows.

3.3. *Evolution of the particulate flow*

3.3.1. *Mean velocity data*

Looking at figures 3(*a*), 4 and 5 or at global vector plots not presented here, we see that the mean flow field of the particulate phase is qualitatively similar to the mean air flow. The mean jet, recirculating and early wake regions are evidenced. However, quantitative differences are significant and are analysed below.

Particles are introduced in the inner jet flow region. They have initially a slight negative mean relative velocity (figure 3*a*). They are accelerated by the gas along the potential core and reach the mean gas velocity. Further downstream, the glass beads have to adjust to the strong longitudinal decrease of air velocity. The associated timescale $\tau_{dec} = 15$ ms is small. Most particles are, therefore, only partly responsive. They lag the fluid behaviour and their mean axial velocity decrease more slowly. The difference induced by particle inertia is particularly striking just downstream of the first stagnation point. At this location, small and large size classes exhibit mean longitudinal and radial velocities of opposite sign near the axis (figures 4 and 5).

Owing to the timescale analysis, the smallest 20 μm particles of Stokesian timescale $\tau_{p20} = 3$ ms should follow closely the fluid motion in the jet region. This is not reflected in figures 3 and 4 where a non-negligible mean velocity difference with air ($\langle U_p \rangle_{p20} - \langle U_f \rangle_f$) is measured. It is, however, important to keep in mind that particles are only added to the inner jet flow. This velocity difference is therefore not the mean velocity difference ($\langle U_p - U_f \rangle_{p20}$) seen by 20 μm particles. In single-phase flow, velocity measurements conditional on fluid originating from either the inner jet or the annular air have been performed by Scheffer *et al.* (1987) by seeding only one of the originally separated flows. Large differences between conditional measurements have

been found in the stagnation region. These results can be interpreted as the signature of random passage of partially mixed large structures through the measurement volume, some originating from the inner jet, the others from the annular flow. Large negative upstream velocities are associated with the annular air flow, and the mean velocity consists of a complex average of the contributions from the conditional data. The velocity conditional on the inner jet is thus obviously larger than both velocity conditional on annular jet and mean fluid velocity in the recirculating region. If small particles are assumed to follow closely the large-scale motion of the fluid conditional on the inner jet, the measured particle mean velocity and the fluid velocity seen by these particle should be identical with $\langle U_p - U_f \rangle_{p20} \approx 0$. The behaviour of small responsive particles at moderate mass loading emphasizes the large-scale intermittency characteristic of this stagnating jet flow. The predictions of numerical calculations will be very dependant on the modelling of fluid/particle correlated motion in this situation. In computing the mean momentum exchange between the fluid phase and the particles, it is important to model accurately the evolution of the mean drift velocity $Vd = (\langle U_f \rangle_p - \langle U_f \rangle_f) = \langle u_f \rangle_p$ (Simonin 1991). For $20\,\mu\mathrm{m}$ responsive particles, Vd_{20} is positive and far from being negligible. On the other hand, particles belonging to larger size classes should become uncorrelated with the presence of the jet fluid because of their inertia. The value of their drift velocity will therefore tend toward zero. These aspects are presently analysed in more detail by using the method introduced by Prévost *et al.* (1996) to deduce the fluid statistics seen by the particles.

At all axial locations displayed in figures 4 and 5, we note that the mean movement of the large particles differs significantly from the mean movement of the fluid in the outer region. Their mean longitudinal velocities are significantly lower than the fluid velocity. As particles are introduced in the central region only, we feel that the presence of large particles is associated mainly with outward fluid motion of low longitudinal velocity. Indeed, an outward mean motion of the large classes is measured at the corresponding radial locations. Again, these results show that particles provide a signature of the large-scale intermittency characteristic of the recirculating bubble. Note, however, that the statistical convergence associated with large particles in the outer region ($r > 80\,\mathrm{mm}$) is poor because fewer than 200 samples were used to limit duration of data acquisition.

3.3.2. *Fluctuating velocity data*

The radial evolutions of the particle kinetic stresses near the axis at $x = 80\,\mathrm{mm}$ (figures 6, 7 and 8) are typical for an early jet region. Previous studies (Modaress *et al.* 1984; Hardalupas *et al.* 1989; Prévost *et al.* 1996) have already shown the noticeable anisotropy between the axial and radial fluctuating velocities in free shear flows. This difference arises from the production of particle streamwise turbulence by mean particle velocity radial gradients while particle velocity radial fluctuations should be controlled mostly by the dragging by the fluid turbulent motion (Simonin 1991). The anisotropy of the particle fluctuating motion increases further in the jet-stagnation region. A clear maximum of the axial fluctuating velocity of the particle is detected in figure 3(*a*). This maximum corresponds to the location of maximum production of u'_p by mean longitudinal velocity gradients (see Simonin *et al.* 1995 for the corresponding equations). This maximum is clearly shifted downstream of u'_f maximum. This observation is emphasized in figure 6 where the longitudinal fluctuating velocity of the particles is seen to exceed the fluid value in the near axis region. The influence of inertia is therefore dominant in driving these production effects and no local equilibrium with the fluid turbulence can be assumed when
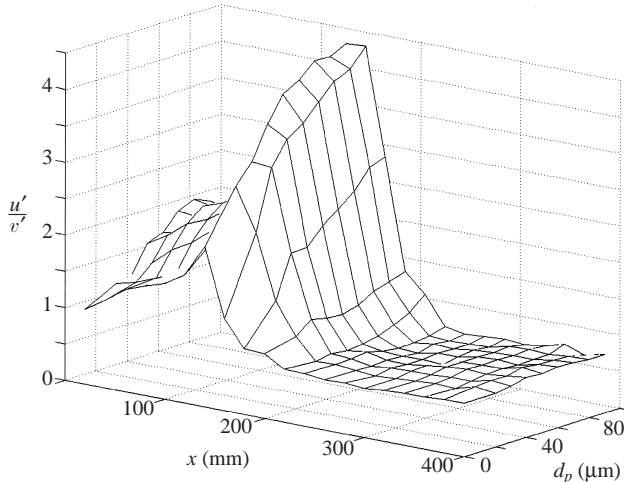
FIGURE 12. Surface plot of the axial evolution of the ratio u'/v' as a function of the size class ($M_j = 22\%$).

modelling such flows. The radial profiles of figure 6 show that u'_p is locally minimum in the recirculation. The signature of shear production in the outer shear layer is again very clear. Note that both u'_p and $\langle uv \rangle_p$ are larger than the corresponding fluid values in the outer region for $d_p \geqslant 40 \, \mu\text{m}$. The radial profile of v'_p (figure 7) exhibits a clear off-centre maximum which again coincides with a maximum production of v'_p.

A surface plot of the axial evolution of the ratio u'_p/v'_p as a function of the size class is presented in figure 12. Although qualitative in nature, this graph shows the steep increase of the anisotropy as d_p increases. A peak value $u'_p/v'_p = 4.4$ is reached for large glass beads at $x = 160 \, \text{mm}$. In this graph, we see that u'_p/v'_p increases continuously in the jet flow region. However, a sharp transition occurs when we move downstream of the first stagnation point. This transition is not surprising as we know that particles recirculate before entering the downstream end of the separated bubble. In describing the evolution of the continuous phase (§3.1), we have seen that the driving physical mechanisms and the associated timescales in the recirculating and early wake flow differ markedly from the jet-flow region. Figure 3(c) shows clearly that the shaking of the glass beads by the large eddies flowing downstream of the separated region results in an increase of radial r.m.s. velocity v'_p whatever the size class at about $x = 200 \, \text{mm}$. v'_p reaches a maximum at the axial location corresponding to the end of the recirculating region. A slow decrease of the radial r.m.s. velocity is then measured in the early wake flow. Noticeably, figure 12 shows that the anisotropy $u'_p/v'_p \approx 0.7$ is then very similar to the fluid one whatever the size class. This observation seems to indicate that the particle velocity fluctuations are controlled mostly by the dragging by the large-scale fluid turbulent motion in this region.

3.4. *On the estimation of non-Stokesian effects*

High values of the mean drift velocity and large fluctuating velocities are measured in this flow. Non-Stokesian effects (Anderson & Longmire 1995) are therefore expected to have a significant influence. The increase in drag coefficient, as Reynolds number increases, decreases the particle time constant. In a laminar flow, for the particle class i, the modified time constant used currently for Reynolds number up to 800 is (Crowe,

Size class (μm)	40	60	80
Mean modulus $\langle\|U_p - U_f\|\rangle_p$ (m s^{-1})	2.5	2.7	2.9
Reynolds number Re_p	6.4	10.4	14.8
Stokes time constant τ_{pST} (ms)	12	27	47
Modified time constant τ_p (ms)	8	15	24
Froude number Fr_p	33.2	18.1	12.2

TABLE 2. Local particle parameters on the axis at $x = 160$ mm near the particle mean stagnation point ($M_j = 22\%$).

Sommerfeld & Tsuji 1998):

$$\tau_{pi} = \frac{\tau_{piST}}{\left[1 + 0.15 Re_{pi}^{0.687}\right]} \quad \text{where } \tau_{piST} = \frac{\rho_p d_{pi}^2}{18\mu}. \tag{3.2}$$

In a turbulent flow, Simonin *et al.* (1995) have shown that a simple model for the nonlinear dependence of the drag coefficient can be used in (3.2) where Re_{pi} is based on the local mean value of the modulus of the relative velocity $\langle\|U_p - U_f\|\rangle_{pi}$. However, it is difficult to estimate this mean value in an experiment. Fessler & Eaton (1999) propose a list of different velocity scales based on mean velocity difference or fluctuating velocities. They evaluate a characteristic particulate Reynolds number which is supposed to be a valid estimation over all the backward-facing step flow. We prefer to compute local values in the present work because the bluff-body flow is strongly inhomogeneous. As an illustration, our goal is to compare the response of the particles on axis in both stagnation regions. An important point is then to deduce the magnitude of gravity effects from these estimations.

On the axis of the flow, Re_{pi} reduces to:

$$Re_{pi} = \frac{d_{pi}}{v}\sqrt{\langle U_p - U_f\rangle_{pi}^2 + \langle(u_p - u_f'')^2\rangle_{pi} + 2\langle(v_p - v_f'')^2\rangle_{pi}}, \tag{3.3}$$

u_f'' is defined by $u_f'' = U_f - \langle U_f\rangle_{pi}$. $\langle U_f\rangle_{pi}$ is the mean fluid velocity seen by the particle class i. $\langle u_f'' u_f''\rangle_{pi}$ (where $\langle u_f''\rangle_{pi} = 0$) is the fluid turbulent Reynolds stress seen by the particles. We assume that $\langle u_f'' u_f''\rangle_{pi} \approx \langle u_f u_f\rangle_f$ (Simonin *et al.* 1995). $\langle u_p u_f''\rangle_{pi} = \langle u_p U_f\rangle_{pi} = \langle u_p u_f\rangle_{pi}$ corresponds to the fluid particle velocity correlations (similar definitions are, of course, associated with the radial velocity component). An estimation of these correlations is necessary for the present purpose.

The respective values of Re_{pi}, τ_{pi} and St_i near the mean stagnation point of the laden jet are estimated in table 2 for size classes 40, 60 and 80 μm. The larger particles are partly responsive. We suppose for this order of magnitude analysis that $\langle U_f\rangle_{pi} \approx \langle U_f\rangle_f$. As S_1 is concerned, we have shown in the previous section that the production of longitudinal particle fluctuating velocity is very significant in this region. We thus assume that $\langle u_f u_p\rangle_{pi} \ll \langle u_p u_p\rangle_{pi}$ and that $\langle u_f u_p\rangle_{pi} \ll \langle u_f u_f\rangle_f$ which leads to $\langle(u_p - u_f'')^2\rangle_{pi} \approx \langle u_p^2\rangle_{pi} + \langle u_f^2\rangle_f$. On the contrary, the radial component of the fluctuating motion of the particles being mainly controlled by the dragging by the fluid turbulence, we suppose accordingly that $\langle v_f v_p\rangle_{pi} \approx \langle v_p v_p\rangle_{pi}$ which leads to $\langle(v_p - v_f'')^2\rangle_{pi} \approx \langle v_f^2\rangle_f - \langle v_p^2\rangle_{pi}$.

In table 2 (and table 3 discussed below), the major contribution to the mean drift modulus is due to the fluctuating terms. We see that the correction for non-negligible Reynolds number is very significant but that large particles remain only partly responsive to the deceleration. Note that Re_{p60} and Re_{p80} are larger than 10.

Size class (µm)	40	60	80
Mean modulus $\langle \| \boldsymbol{U}_p - \boldsymbol{U}_f \| \rangle_p$ (ms^{-1})	1.0	1.2	1.4
Reynolds number Re_p	2.6	4.6	6.9
Stokes time constant τ_{pST} (ms)	12	27	47
Modified time constant τ_p (ms)	9	19	30
Froude number Fr_p	11.3	6.6	4.6

TABLE 3. Local particle parameters on the axis at $x = 240$ mm near the second stagnation point S_2 ($M_j = 22\%$).

The flow distortion in the wakes of particles should therefore extend along many particle diameters (Fessler & Eaton 1999).

From these estimations, it is possible to deduce whether gravity is an important contribution to the motion of the glass beads in this region of the vertically downward flow. A Froude number $Fr_{pi} = \langle \| \boldsymbol{U}_p - \boldsymbol{U}_f \| \rangle_{pi} / \tau_{pi} g$ is defined in Hardalupas *et al.* (1992). Fr_{pi} is the ratio of the magnitude of the mean drag force to the weight of the particle i. Looking at table 2, we see that Fr_{pi} is larger than 10 for all particle size classes. Gravity effects are therefore not expected to be significant near S_1.

Particle dimensionless parameters near the mean stagnation point S_2 are displayed in table 3. Predictions of fluid/particle correlated motion in the framework of Tchen theory (Hinze 1975) have been used to estimate both axial and radial fluid particle velocity correlations with $\langle u_f u_p \rangle_{pi} \approx \langle u_p u_p \rangle_{pi}$ and $\langle v_f v_p \rangle_{pi} \approx \langle v_p v_p \rangle_{pi}$. Table 3 shows that most particle classes are responsive to the fluid turbulence in this region and that the influence of gravity is small.

4. Comparative description of the polydispersed flow field at high mass loading

In single-phase flow and for a given geometry, numerous studies of bluff-body stabilized flows have shown that a major control parameter is the momentum flux ratio MR. Namazian *et al.* (1992) show how mixing and flame behaviour are strongly influenced by this parameter. $MR = \rho_j \overline{U_j}^2 / \rho_e \overline{U_e}^2$ compares the momentum flux of the inner jet to the momentum flux of the annular jet (see e.g. Chen *et al.* 1990). A low value of MR corresponds to an inner jet that stagnates and mixes in the recirculating zone. This situation is the present single-phase configuration characterized by $MR = 0.69$. For high values of MR, the jet penetrates through the recirculating region.

In the presence of glass beads, the value of the mass loading M_j provides information about the proportion of the momentum flow rate carried by the particles to that carried by the gaseous phase in the inner jet. The momentum flux ratio reads: $MR = (1 + M_j) \overline{U_j}^2 / \overline{U_e}^2$. $MR = 0.84$ at $M_j = 22\%$, and $MR = 1.44$ at $M_j = 110\%$. M_j is therefore expected to have a strong effect on the downstream evolution of the recirculating region. A direct analogy with single-phase flow would, however, only be possible for fully responsive particles whose characteristic time of momentum exchange is much smaller than the flow timescales. The present situation is more complex as most particles are only partly responsive.

One of our main objectives in this study was to show that the sensitivity to mass loading deeply affects the dispersion of the glass beads and that an accurate prediction of two-way coupling is crucial when modelling this kind of situation. The two-phase
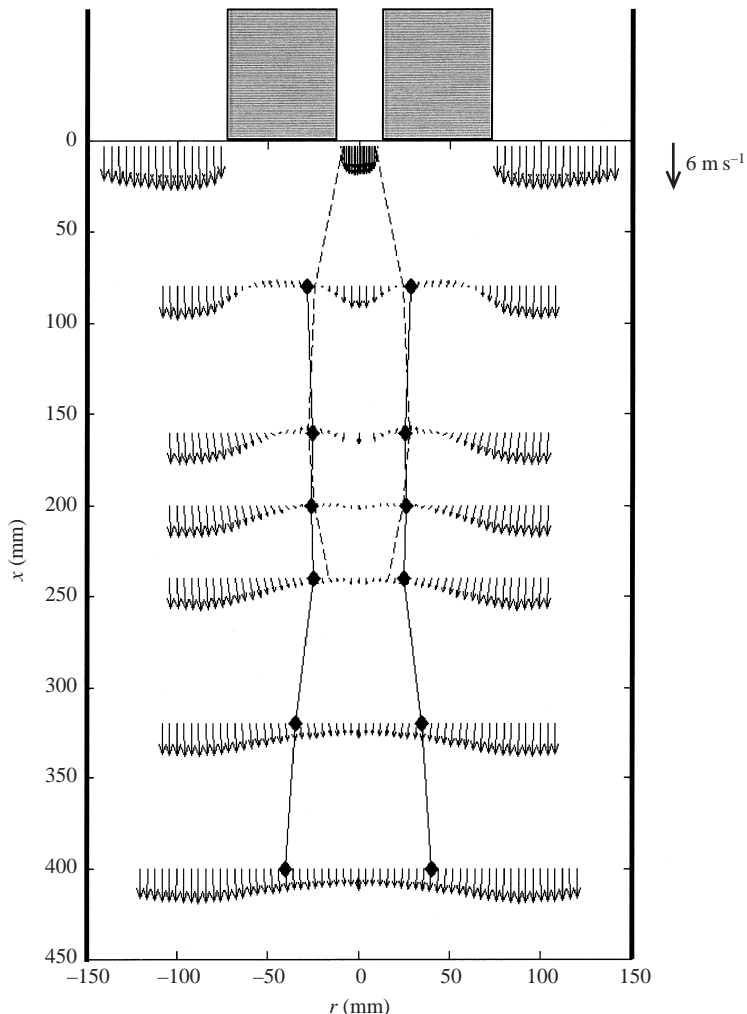
FIGURE 13. Vector plot of the mean gas flow at $M_j = 110\%$. ◆, mean distance from axis (equation (3.1)) for 60 μm particle size class. — — —, flow region where $N_{C60} \geqslant 1$, i.e. where particle/particle collisions are probable for 60 μm particle size class (see § 5).

flow measured at $M_j = 110\%$ is described in the following and compared with the previous results. The modification of the fluid turbulence induced by the presence of particles is discussed in § 4.3.

A vector plot of the mean air flow field in the presence of glass beads at $M_j = 110\%$ is presented in figure 13. The longitudinal evolution of the mean distance from axis R_{p60} (equation (3.1)) is superimposed on the same plot. In order to compare both situations quantitatively, axial evolutions and radial profiles of mean and r.m.s. quantities are provided in figures 14 and 15. Location $x = 160$ mm was selected for this comparison because it corresponds to a mean recirculating region on the axis in single-phase flow and at $M_j = 22\%$. The database (Ishima *et al.* 1999) gives the complete set of data.

Note that the inlet boundary conditions, and particularly the two-phase flow at the exit of the central tube, were carefully measured both to understand some features
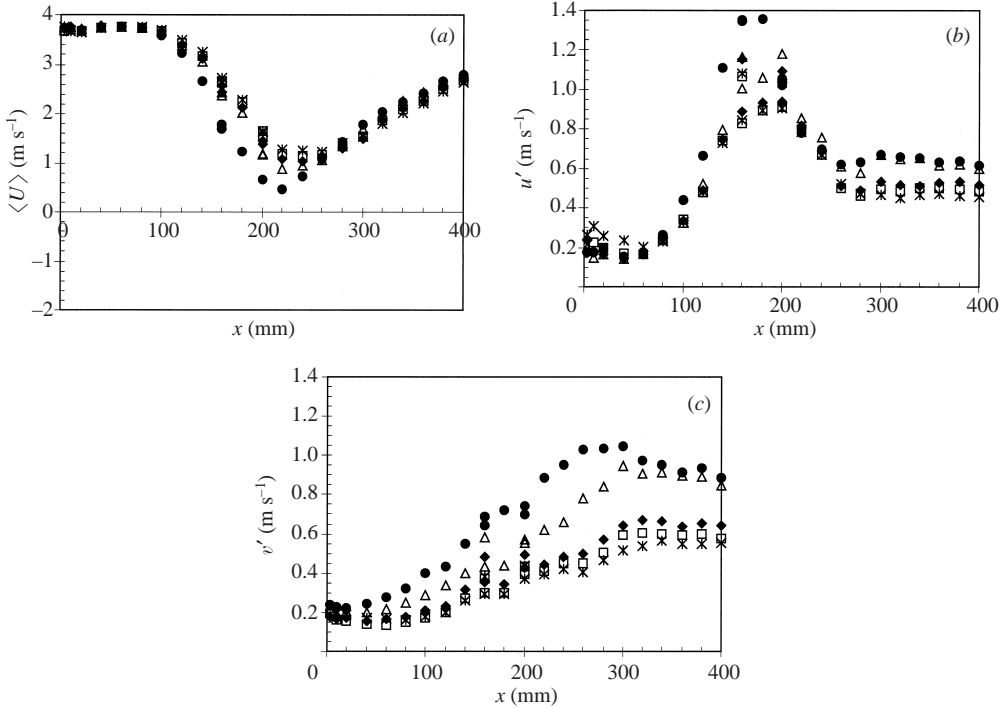
FIGURE 14. Axial evolution of the mean and r.m.s. velocity of continuous and dispersed phase at $M_j = 110\%$. ●, tracers; △, $d_p = 20\,\mu\text{m}$; ◆, $d_p = 40\,\mu\text{m}$; □, $d_p = 60\,\mu\text{m}$; ✳ $d_p = 80\,\mu\text{m}$. (a) Mean longitudinal velocity; (b) r.m.s. longitudinal velocity; (c) r.m.s. radial velocity.

of the downstream evolution and to build a useful database. In the tube flow, the influence of the response time of the particles is noticeable. Mean and fluctuating velocity profiles are strongly dependent on the size class. A complex effect of mass loading on second-order moments of the continuous phase is observed. Clear links with the nature of the tube turbulence are evidenced in an ongoing analysis and will be the subject of a separate paper.

4.1. *Particle dispersion at $M_j = 110\%$*

A visual comparison between figures 2 and 13 shows immediately that two-way coupling is responsible for a spectacular change in particle dispersion. The mean distance from the axis, which is a global measure at a given axial position, is significantly smaller. For example, at $x = 80\,\text{mm}$, R_{p60} is 1.7 times smaller at $M_j = 110\%$ than at $M_j = 22\%$. A slight ($\approx 10\%$) decrease of the mean distance from the axis is detected along the recirculating region. Radial dispersion appears to increase significantly in the early wake region only. The contrast between the two situations is evident if one looks back at the profiles displayed in figures 9 and 10. Figure 9(a) shows that the relative mean longitudinal mass flux directed upstream in the off-axis recirculation and downstream in the outer shear layer is much weaker at the highest loading. The relative mean mass concentration in the recirculating bubble is smaller and no maximum is detected in the outer shear layer (figure 11a). Noticeably, at $M_j = 110\%$, figures 9(b) and 10(b) show that a strong decrease of near-axis mass flux and concentration occurs at the end of the off-axis-recirculated region where an efficient dispersion begins. The signature of the jet is, however, detected far
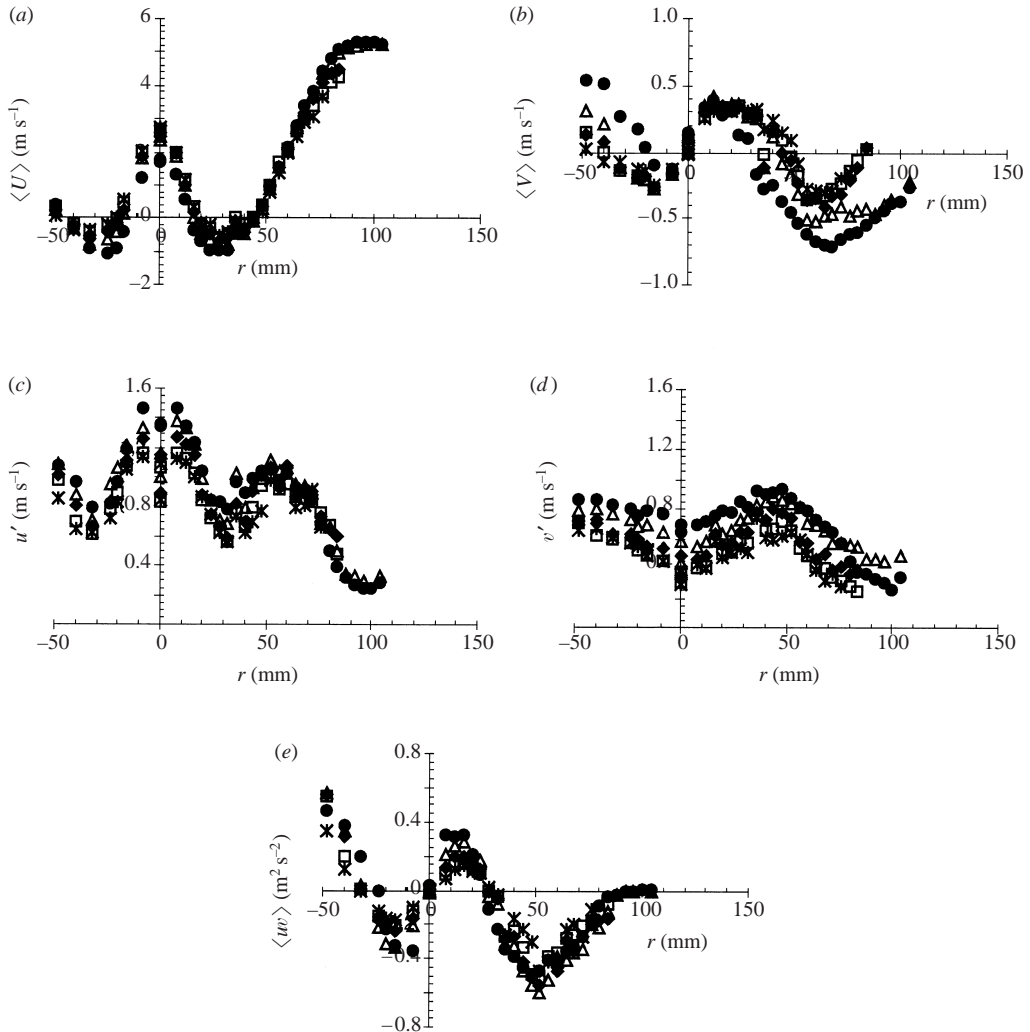
FIGURE 15. Radial profiles of the two-phase flow at $x = 160\,\text{mm}$. $M_j = 110\%$. ●, tracers; △, $d_p = 20\,\mu\text{m}$; ■, $d_p = 40\,\mu\text{m}$; □, $d_p = 60\,\mu\text{m}$; ✳ $d_p = 80\,\mu\text{m}$. (*a*) Mean longitudinal velocity; (*b*) mean radial velocity; (*c*) axial fluctuating velocity; (*d*) radial fluctuating velocity; (*e*) Reynolds shear stress.

downstream. These results show the interest of configurations with a stagnation point on the axis.

Detailed mean mass frequency distributions have been analysed at representative locations of this flow. On the axis, we observe a continuous shift of the mean mass frequency distribution toward large size classes. Inertia effects which are more pronounced for large size classes in the turbulence of the penetrating jet are responsible for this observation. Noticeably, mass frequency distributions drawn at the same axial locations but at $r = 76\,\text{mm}$, i.e. aligned with the edge of the bluff body in the outer shear layer, show an opposite trend with a continuous shift of the mean mass distribution toward small size classes that disperse more efficiently. At the exit of the measurement domain ($x = 400\,\text{mm}$) and at $M_j = 110\%$, the mass averaged diameter of the polydispersion is $\overline{d_{pM}} = 65\,\mu\text{m}$ on the axis and $\overline{d_{pM}} = 59\,\mu\text{m}$ at $r = 76\,\text{mm}$. The
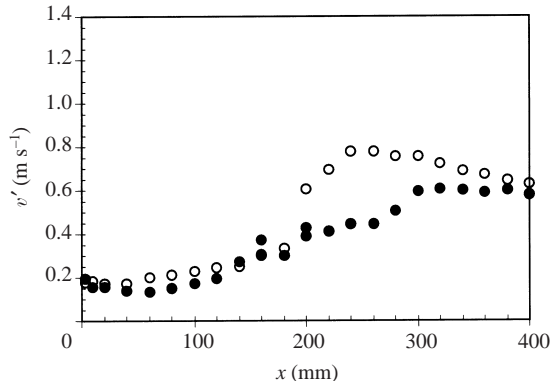
FIGURE 16. Comparison of the axial evolution of v'_{p60} at the two mass loading. ○, $M_j = 22\%$; ●, $M_j = 110\%$.

important changes in the particle dispersion observed here are very important for applications in practical devices. The contrasted observations are also believed to be of interest to test the recent developments in two-phase flow modelling. The results obtained numerically should indeed be very sensitive to the accurate description of the physical processes involved.

4.2. *Evolution of the air and particle flow fields*

A direct comparison of the radial evolutions of the air properties in single-phase flow and at both mass loading (not displayed here for brevity) shows that the flow properties in the external shear region of the recirculation bubble have not changed significantly. The major differences at high mass loading concern the central region. The signature of the mean air jet is particularly clear on the radial profiles at $x = 160$ mm (figure 15*a*). A mean recirculation zone develops off-axis only. The fluid and particles flow radially outward in the central region. Comparing the axial evolutions of the mean axial velocities in figure 14(*a*) with figure 3(*a*), we see that the length of the potential core increases with mass loading and that the region of strong velocity decrease is shifted downstream. The corresponding fluid timescale is now $\tau_{dec} = (\partial \langle U_f \rangle_f / \partial x)^{-1} \approx 28$ ms. Particles still lag the fluid behaviour. However, the different size classes now clearly respond in a very similar way whatever their response time. In figure 14(*a*), no mean stagnation point is detected on the axis for $M_j = 110\%$. The particle-laden jet therefore penetrates through the recirculating region.

Figure 14(*b*) shows that the downstream increase of longitudinal fluctuating velocity at the exit of the inner jet is delayed at the highest mass loading. The location of the peak of axial r.m.s. velocity is also shifted downstream, together with the shift of maximum longitudinal gradient of the mean axial velocity. It is interesting to compare the axial evolution of the radial fluctuating velocity at both loadings (figures 3*c* and 14*c*). In both cases, the initial increase of v'_p is slow, particularly for the largest size classes. v'_p increases continuously and reaches a maximum at the axial location corresponding to the end of the recirculating region. These regions include the axis at $M_j = 22\%$, but are located off-axis at $M_j = 110\%$. A slow decrease of the radial r.m.s. velocity is then measured in the early wake flow. A closer look at figures 3(*c*) and 14(*c*) brings major differences to light as both mass loadings are concerned. Figure 3(*c*) shows that v'_p increases sharply whatever the size class in the recirculation zone
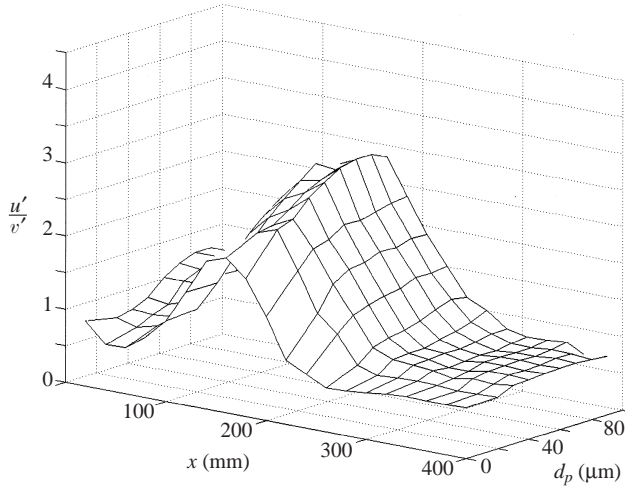
FIGURE 17. Surface plot of the axial evolution of the ratio u'/v' as a function of the size class
($M_j = 110\%$).

about $x = 200$ mm. Such a sharp increase is not observed at the highest mass loading
(figure 14c). To emphasize this point, the axial evolution of radial fluctuating velocities
of 60 µm size classes are compared in figure 16. This comparison is representative of
all size classes. The sharp increase and high level of v'_p at the lowest mass loading is
associated with the recirculation of the glass beads. This effect is not observed at the
highest mass loading because the jet penetrates through the recirculation zone.

A surface plot of the axial evolution of the ratio u'_p/v'_p as a function of the size class
is presented in figure 17. The anisotropy increases continuously in the jet region, but
levels-off surprisingly for the large size classes ($d_p \geqslant 50$ µm). A peak value $u'_p/v'_p = 3.0$
is reached for these classes. The value of the anisotropy and its size evolution in the
jet region are thus very different at both mass loadings (compare with figure 12). Both
evolutions are, however, very similar in the early wake region where the dragging by
the large-scale fluid motion dominates.

4.3. *Discussion concerning turbulence modification by particles in the bluff-body flow*

A large modification of the fluid turbulence is induced by the presence of the particles
in the bluff body flow. The longitudinal evolutions of the radial profile of u'_f in single-
phase situation and at both mass loadings are compared in figure 18. The changes
occur in the jet and recirculation region. At the jet exit, the axial fluctuating velocity
of the air is damped and the magnitude of the peak of u'_f is more than 40% lower
at $M_j = 110\%$ than at $M_j = 22\%$. Surprisingly, and contrary to the classical results
of Kulick *et al.* (1994), no attenuation of u'_f is detected near the axis of the tube.
This behaviour is currently under investigation. Measurements performed at the same
location, but at intermediate mass loading show an attenuation of u'_f on the axis when
M_j is increased up to 60%. The longitudinal turbulent intensity then increases again
as the loading ratio increases further and reaches almost the same value as in the
single-phase flow. Such evolution is observed, but not explained, in Tsuji *et al.* (1984)
for their smallest particle size class. It is also reported in the early work of Maeda,
Hishida & Furutani (1980).

Further downstream along the jet, at $x = 80$ mm, the peak values of u'_f in the shear
layer are approximately the same. However, the longitudinal turbulent r.m.s. velocity
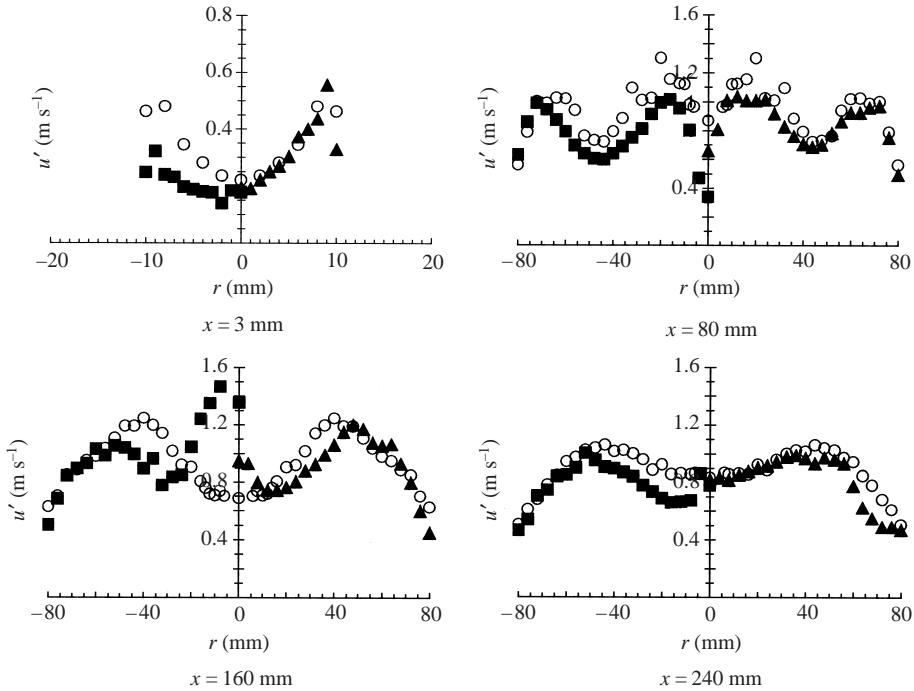
FIGURE 18. Comparison of the longitudinal evolutions of the radial profile of u'_f in single phase situation and at both mass loadings. $\bigcirc$, Single phase; $\blacktriangle$, $M_j = 22\%$; $\blacksquare$, $M_j = 110\%$. Note that the scale of ($x = 3$ mm) plot is expanded to show the trends discussed.

of the fluid is much lower in the core of the jet at high mass loading. This observation is confirmed by comparing the axial evolutions in figures 3(*b*) and 14(*b*). Finally, modifications of the turbulent field are detected in the central region at $x = 160$ mm and $x = 240$ mm where the jet interacts with the downstream end of the recirculation zone.

As modelling issues are concerned, the transport equation for turbulence kinetic energy with two-way coupling are found for example in Kulick *et al.* (1994). A direct fluid–particle interaction term Π (discussed below) complements the conventional terms of the equation for single phase flows. As discussed in §1, the picture of turbulence modification by particles is extremely complex and involves direct and indirect mechanisms. In the present inhomogeneous flow of non-uniform particle mass loading, large indirect changes obviously occur through modifications of the mean fluid flow. Our goal is to show that the direct effect is significant by comparing the production of longitudinal fluctuating component u'_f, i.e. the major source of turbulent kinetic energy in the inner jet flow, with the associated fluid–particle interaction term $\Pi_{u'_f}$.

We use the transport equation for the turbulent stress tensor established in Simonin *et al.* (1995) and Vit *et al.* (1999):

$$\frac{D\langle u_f u_f \rangle_f}{Dt} = \frac{D\langle u_f u_f \rangle_f}{Dt}\bigg|_{SP} + \Pi_{u'_f}. \tag{4.1}$$

In (4.1), the first term on the right-hand side represents the conventional equation for single-phase flows (index SP). For each class of particles much heavier than the surrounding gas and whose size is small with respect to the fluid turbulent energetic

lengthscales, the work performed by the turbulence in shaking the glass beads is:

$$\Pi_{u_{f'},j} = 2\frac{\rho_p \alpha_j}{\rho_f \alpha_f}\frac{1}{\tau_{pj}}\langle (U_p - U_f)u_f\rangle_{pj}$$

$$= 2\frac{\rho_p \alpha_j}{\rho_f \alpha_f}\frac{1}{\tau_{pj}}(\langle u_f u_p\rangle_{pj} - \langle u_f u''_f\rangle_{pj} + \langle u_f\rangle_{pj}\langle U_p - U_f\rangle_{pj}), \quad (4.2)$$

α_j is the volumetric fraction for class j: $\alpha_j = (\pi d_j^3/6)C_j$, α_f is the fluid volumetric fraction: $\alpha_f = 1 - \sum_{class}\alpha_j \approx 1$. $U_f = \langle U_f\rangle_{pj} + u''_f$ with $\langle u''_f\rangle_{pj} = 0$. Thus, $\langle u_f u''_f\rangle_{pj} = \langle U_f u''_f\rangle_{pj} = \langle u''_f u''_f\rangle_{pj}$. This corresponds to the fluid turbulent Reynolds stress seen by the particles. Summing all the size classes, we obtain:

$$\Pi_{u'_f} = \frac{2}{\rho_f \alpha_f}\sum_{classes}\frac{\rho_p \alpha_j}{\tau_{pj}}(\langle u_f u_p\rangle_{pj} - \langle u''_f u''_f\rangle_{pj} + \langle u_f\rangle_{pj}\langle U_p - U_f\rangle_{pj}). \quad (4.3)$$

Very little is known about (4.3) when partly responsive particles are concerned, and this is clearly the case in the present work. Simultaneous measurements of fluid and particle motion using laser techniques (Prévost *et al.* 1996; Hishida & Sato 1998; Longmire *et al.* 1999) are present challenges to reach a better understanding when it is not possible to neglect the influence of fluid/particle correlations that contribute to reduce the magnitude of $\Pi_{u'_f}$.

To check that $\Pi_{u'_f}$ is significant when compared to the production term, and to prove that direct interaction with turbulence has to be taken into account explicitly by modelling attempts, we will restrict ourselves to the jet shear region where fluid/particle correlation can be modelled accurately by using recent theoretical results. The maximum shear rate at $x = 80\,\text{mm}$ is measured at the radial distance $r = 12\,\text{mm}$ with $S = -220\,\text{s}^{-1}$ at $M_j = 22\%$ and $S = -264\,\text{s}^{-1}$ at $M_j = 110\%$. In a particle-laden jet flow, the experimental work of Prévost *et al.* (1996) shows that the longitudinal drift velocity $\langle u_f\rangle_p$ is negligible. Moreover, if the contribution of mean advection and turbulent diffusion of $\langle u_p u_p\rangle_p$ is neglected in the high-shear region of the jet, the transport equation for $\langle u_p u_p\rangle_p$ written by Simonin *et al.* (1995) leads to the following approximate relation between the dominant production term and the interphase momentum transfer rate:

$$-2\langle u_p v_p\rangle_{pj}\frac{\partial U_{pj}}{\partial r} - \frac{2}{\tau_{pj}}(\langle u_p u_p\rangle_{pj} - \langle u_f u_p\rangle_{pj}) \approx 0 \Rightarrow \langle u_f u_p\rangle_{pj} \approx \langle u_p u_p\rangle_{pj} + \tau_{pj}\langle u_p v_p\rangle_{pj}\frac{\partial U_{pj}}{\partial r}.$$
$$(4.4)$$

As stated by Simonin *et al.* (1995), equation (4.4) satisfies the classical result $\langle u_f u_p\rangle_{pj} \approx \langle u_p u_p\rangle_{pj}$ obtained in the framework of Tchen theory (Hinze 1975) for fully responsive particles. For partly responsive particles, the contribution of mean production implies that the streamwise particle velocity variance is higher than the corresponding fluid/particle velocity correlation. Equation (4.3) can thus be evaluated from our measurement set by using the modelled form of fluid/particle velocity correlation (4.4). The non-Stokesian correction for τ_{pj} (equation (3.2)) is taken into account. To be complete, we compare the results displayed in table 4 with the estimation of the attenuation term usually found in the literature and obtained when $\langle u_f u_p\rangle_{pj}$ are neglected:

$$\Pi^*_{u'_f} = -\frac{2}{\rho_f \alpha_f}\sum_{classes}\frac{\rho_p \alpha_j}{\tau_{pj}}(\langle u_f u_f\rangle_f). \quad (4.5)$$

Two important conclusions are obtained from table 4. First, we see that direct

	$P_{u'_f}(\mathrm{m^2\,s^{-3}})$	$\Pi_{u'_f}(\mathrm{m^2\,s^{-3}})$	$\Pi^*_{u'_f}(\mathrm{m^2\,s^{-3}})$
$M_j = 22\%$	113	−9	−16
$M_j = 110\%$	135	−58	−85

TABLE 4. Comparison of production and attenuation of longitudinal fluctuating component u'_f in the maximum shear region of the jet ($x = 80\,\mathrm{mm}$; $r = 12\,\mathrm{mm}$).

Size class (μm)	20	40	60	80
$S\tau_{pj}$	0.68	2.38	4.84	7.86
$\langle u_f u_p \rangle_{pj}/\langle u_f u_f \rangle_f$	0.87	0.50	0.26	0.08

TABLE 5. $M_j = 110\%$. Dependence of the longitudinal fluid/particle velocity correlation computed from (4.4) on the mean shear and particle relaxation time product ($S\tau_{pj}$).

attenuation of turbulence by particle is indeed significant. The shear production of u'_f increases at $M_j = 110\%$, but the direct attenuation of turbulence increases accordingly. The sum of $P_{u'_f} + \Pi_{u'_f}$ is reduced by 25% from low to high mass loading. However, this location remains an important source of longitudinal fluctuating component u'_f. Therefore, the very significant decrease of u'_f observed in the core of the jet is probably induced by a modification of the radial turbulent transport terms. Reliable measurements of third-order moments $\langle u_f u_f v_f \rangle_f$ (Caraman *et al.* 2001) are still needed to clarify this point. Secondly, table 4 shows clearly that one key point for the prediction of turbulence attenuation by particles is the prediction of fluid/particle velocity correlations. $\Pi^*_{u'_f}$ really overestimates the magnitude of the attenuation. The ratio $\langle u_f u_p \rangle_{pj}/\langle u_f u_f \rangle_f$ computed via model (4.4) is displayed in table 5. One sees that the mean shear and particle relaxation time product ($S\tau_{pj}$) reaches quite large values. Nevertheless, fluid/particle correlations are important terms. General constitutive relations for fluid/particle velocity correlations restricted to low solid loading ratio were proposed by Fevrier & Simonin (1998). The influence of the fluid turbulence modulation on these quantities is, however, not known.

5. On the probability of particle/particle collisions

The local volume ratio corresponding to the highest mass loading considered here is low – everywhere lower than 0.05%. In such situations, a widely accepted rule of the thumb based on this information only would indicate that particle–particle interactions are negligible. A limit value of 0.3% is, for example, quoted by Hardalupas *et al.* (1989). However, the noticeable mean drift between contrasted size classes and the important turbulent agitation of the particulate phase are clearly expected to favour the occurrence of particle/particle interactions via collisions. If collisions are frequent, the mean and fluctuating characteristics of the different classes are coupled because particles exchange momentum with one another. It is therefore important to analyse the probability of particle/particle collisions. By applying recent applications of kinetic theory to binary mixtures of particles (Gourdel *et al.* 1998, 1999), our goal is to show that accurate numerical collision models are essential for the prediction of such recirculating particle-laden flows.

For monodispersed particulate flows, Eulerian and Lagrangian inter-particle collisions models based on kinetic theory of dense gazes (Berlemont, Simonin & Sommerfeld 1995) are available. A present challenge is to take into account the effect

of preferential concentration and the influence of correlation between colliding particle velocities transported into the same turbulent eddy upon collision (Sundaram & Collins 1997). Elaborate models accounting for the latter effect can be found in Lavieville (1997), Lavieville *et al.* (1997) and Sommerfeld (1999).

In a polydispersed particle-laden flow, the probability of a collision between a particle of size class i and one of class j is more complex to obtain and depends on particle j concentration, particles sizes, mean slip motion and the fluctuating motion of both classes. The importance of collisions for a given size class i is evaluated by computing the ratio N_{Ci} of the averaged time between collisions τ_{Ci} to the particle response time τ_{pi}. $N_{Ci} \leqslant 1$ corresponds to a situation in which collisions cannot be neglected. Only binary collisions are considered here. The frequency of collisions $f_{Ci} = 1/\tau_{Ci}$ is therefore computed as the sum of the frequency of collisions with each size class $f_{Ci} = \sum_{class} f_{Ci,j}$. The correlation of the velocities of colliding particles is not taken into account in the present analysis. Results valid in the kinetic theory limit are used (Abrahamson 1975). To take into account collisions due to fluctuating motion and collisions due to mean drift between particles, $f_{Ci,j}$ is computed as the sum of two asymptotic situations corresponding, respectively, to turbulent fluctuations and low mean drift $f_{TCi,j}$ and to high drift $f_{DCi,j}$ (Gourdel *et al.* 1998) with:

$$f_{Ci,j} = f_{TCi,j} + f_{DCi,j}, \tag{5.1}$$

$$f_{Ci,j} = 2^{2/3} \pi^{1/2} n_j (r_{pi} + r_{pj})^2 \sqrt{\sigma_{pi}^2 + \sigma_{pj}^2}, \tag{5.2}$$

$$f_{DCi,j} = \pi n_j (r_{pi} + r_{pj})^2 \|\langle \boldsymbol{U}_p \rangle_{pi} - \langle \boldsymbol{U}_p \rangle_{pj}\|. \tag{5.3}$$

In (5.2) and (5.3), r_p is the radius of the particle, n_j is the number concentration for class j deduced from mass concentration measurements and σ_{pi}^2 is the averaged fluctuating component: $\sigma_{pi}^2 = \frac{1}{3}(u_{pi}^2 + v_{pi}^2 + w_{pi}^2) \approx \frac{1}{3}(u_{pi}^2 + 2v_{pi}^2)$. This relation is exact on the axis of the axisymmetric flow.

More general but also more complex relations are found in Gourdel *et al.* (1999). The present relations are, however, sufficient for our purpose and allow us to distinguish eventually between two collisional contributions due respectively to turbulence and mean drift (Simonin 1999):

$$f_{Ci} = f_{TCi} + f_{DCi} = \sum_{class} f_{TCi,j} + \sum_{class} f_{DCi,j}.$$

The averaged time between collisions τ_{Ci} at different axial locations is compared in figures 19–21 with the Stokesian timescale of the particles. We note that τ_{Ci} decreases sharply as the diameter of the particle increases. An analysis based on a mean diameter would be inaccurate. At low mass loading (figure 19) and at the exit of the jet ($x = 3$ mm), the role of particle/particle collisions is expected to be of minor importance as only the largest size classes, which have a large inertia and a low number density, collide with other particles. However, the probability of collisions increases on moving downstream and is very high for most classes about the mean stagnation point ($x \approx 160$ mm). Details of the different contributions to the total collision frequency at this location are presented in figure 20. The main contribution to particle/particle collisions is clearly the turbulent term $\tau_{TCi} = 1/f_{TCi}$. The increase of local number density (see figure 10*a*) and fluctuation intensity from $x = 80$ mm to $x = 160$ mm (see figure 3*a*) is therefore driving the collision frequency. Note that the mean drift term $\tau_{DCi} = 1/f_{DCi}$ is a minimum for small size classes
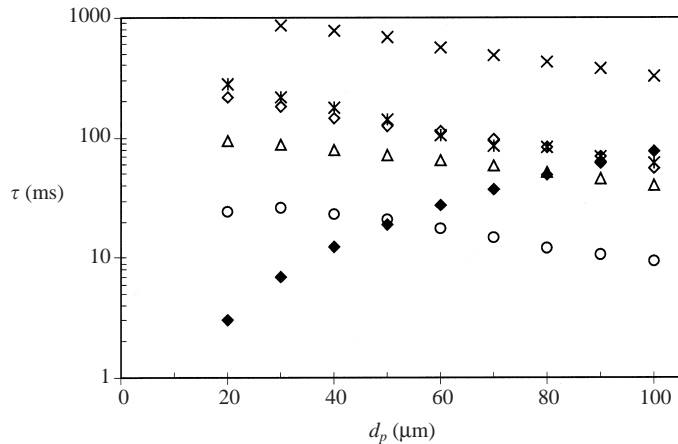
FIGURE 19. Comparison between the average time between collisions and the particle response time at different stations along the axis. $M_j = 22\%$. $\blacklozenge$, τ_{pi}; $*$, τ_{Ci}: $x = 3\,\text{mm}$; $\diamondsuit$, τ_{Ci}: $x = 80\,\text{mm}$; $\bigcirc$, τ_{Ci}: $x = 160\,\text{mm}$; $\triangle$, τ_{Ci}: $x = 200\,\text{mm}$; X, τ_{Ci}: $x = 240\,\text{mm}$.
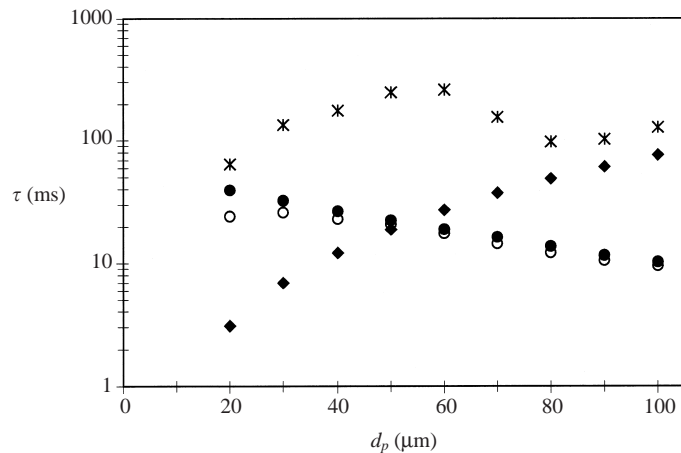

FIGURE 20. $M_j = 22\%$. Details of the different contributions to the total collision frequency at $x = 160\,\text{mm}$. $\blacklozenge$, τ_{pi}; $\bigcirc$, τ_{Ci}; $\bullet$, $\tau_{TCi} = 1/f_{TCi}$ (equation (5.2)); $*$, $\tau_{DCi} = 1/f_{DCi}$ (equation (5.3)).

that present the maximum mean relative velocity. Moreover, τ_{DCi} is maximum for the most probable classes of the polydispersion because the largest number density corresponds to nearby classes and therefore to small mean drift ($f_{DCi,i}$ is for example strictly zero).

Even at low mass loading, major size classes of the polydispersion will therefore experience interparticle collisions in the stagnation region. This is obviously very different from free jet behaviour. However, the region of the flow concerned by collisions is restricted to a very small area about the mean stagnation point. The associated effects on the flow development at the lowest mass loading studied here will therefore be weak.

At $M_j = 110\%$, figure 21 shows that large size classes are expected to be influenced by inter-particle collisions at the jet exit and in the inner jet along all off-axis recirculated region. For all size classes, τ_{Ci} is again much smaller in regions of high fluctuating intensity. Note, however, that the ratio between
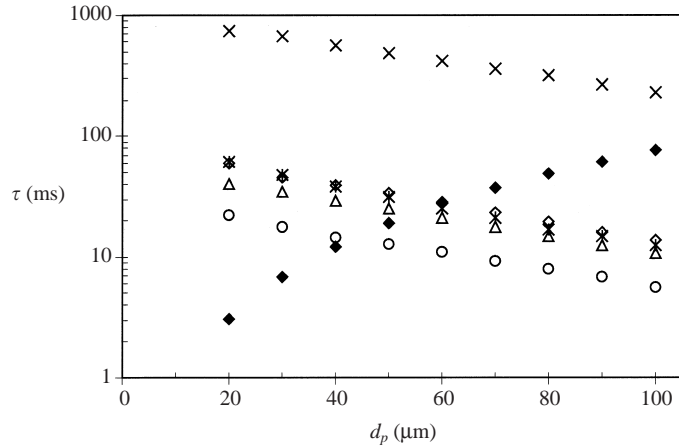
FIGURE 21. Comparison between the average time between collisions and the particle response time at different stations along the axis. $M_j = 110\%$. $\blacklozenge$, τ_{pi}; $*$, τ_{Ci}: $x = 3$ mm; $\diamond$, τ_{Ci}: $x = 80$ mm; $\bigcirc$, τ_{Ci}: $x = 160$ mm; $\triangle$, τ_{Ci}: $x = 240$ mm; $\times$, τ_{Ci}: $x = 320$ mm.

the collision time at the jet exit and the minimum measured τ_{Ci} averaged over all sizes is only $\overline{\tau_{Ci}(x = 3 \text{ mm})/\tau_{Ci}(x = 160 \text{ mm})} \approx 2.5$ at $M_j = 110\%$ whereas $\overline{\tau_{Ci}(x = 3 \text{ mm})/\tau_{Ci}(x = 160 \text{ mm})} \approx 7.3$ at $M_j = 22\%$. A mean stagnation point on the axis thus very clearly favours particle/particle collisions. To provide a global picture, the region of the flow where $N_{C60} \leqslant 1$ at $M_j = 110\%$ is displayed in figure 13. The 'collision domain' obtained by using this order of magnitude comparison would be slightly larger for larger size classes and vanishes for diameter smaller than 40 μm. We see clearly that collisions between a particle of 60 μm and another glass bead is very probable in the inner jet flow. Class to class binary contribution is not detailed in the present paper. However, for this median class of the polydispersion, it is possible to show that most collisions involve a partner of comparative or higher inertia and will therefore have an important effect on the movement.

In the bluff-body flow, (i) the very high level of turbulent fluctuations; (ii) the increase of mean mass concentration if the jet stagnates, and (iii) to a lesser extent the non-negligible inter-class particle mean slip velocity enhance the probability of collisions. One result of the present experiment conducted at two different mass loadings of glass beads is thus that for increasing but moderate mass loading, the region of the particulate flow concerned by collisions will occupy an increasing domain upstream of the mean stagnation region before affecting the whole jet region. It would be interesting to isolate quantitatively the role of collisions on the flow field and the spatial distribution of the dispersed phase. However, we have shown in the previous sections that the increase in M_j is also associated with important modifications of the carrying mean and fluctuating flow. It is therefore impossible to fully separate collisional effects by using the experimental data alone. This extension of the work will involve an interaction with two-phase flow computations in which separate contributions can be artificially isolated. Moreover, the goal of the ongoing work is to obtain detailed data for narrow bidispersed size distribution in order to provide a more quantitative test of the physical models.

According to reference works, collisions should participate to the reduction of mean drift velocity between large classes observed at $M_j = 110\%$. Noticeably, the measured mean drift velocity between 50 and 90 μm particles in the jet region is approximately

three times smaller at $M_j = 110\%$ than at $M_j = 22\%$. Nevertheless, the timescale of the jet velocity decrease is significantly larger at this loading, and both aerodynamical and collision effects therefore combine.

In a polydispersed situation, collisions will also result in a redistribution of fluctuating kinetic energy between all colliding particle classes and between the fluctuating components in a given size class. Again, we have noticed previously (compare figures 12 and 17) that the anisotropy of large classes turbulence is much smaller at the highest loading.

Finally, theoretical studies in homogeneous particle clouds prove that collisions reduce the dispersion of particles because the mean free path is reduced (Lavieville 1997). Neither velocity field nor concentration field are homogeneous in the jet region, but dispersion is expected to be reduced in the core of the jet at high mass loadings of particles. The predictions of these effects are of course very important for applications and are the subject of present developments.

6. Conclusion

The effect of mass-loading on the development of the polydispersed two-phase flow downstream of a confined bluff body was discussed in this paper. The bluff-body flow configuration is one of the simplest turbulent recirculating flows. It is also relevant for applications and forms the basis of numerous combusting devices.

The present data were obtained for isothermal conditions by using a phase-Doppler anemometer allowing size and velocity measurements. A large particle size distribution is introduced into the flow. The statistical properties of narrow particle size classes are displayed and analysed in order to respect the wide range of particle relaxation times. The data presented here form the basis of a validated data set available for model testing. The mean and fluctuating airflow in the presence of glass beads and the statistical properties of the dispersed phase motion is discussed. The evolution of mass fluxes and mass concentration per size class are estimated from the PDA data. Such information is very difficult to obtain in complex three-dimensional flows of high-turbulence intensity. A correction is introduced to ensure that the mass flow rate of particles per size class obtained by integration from the data is correct.

We have shown that the development of the continuous phase is very sensitive to initial mass loading of the inner jet. An increase in mass loading corresponds to an increase in momentum flux ratio between the central jet and annular flow. In the present situation, this implies a complete reorganization of the recirculation zone and of the turbulent field. At $M_j = 22\%$, the momentum ratio is smaller than one and the jet stagnates in the recirculation region; at $M_j = 110\%$, the jet penetrates through the recirculating zone. No accurate prediction of this particle-laden flow can therefore be achieved without considering two-way coupling for the partly responsive glass beads. A large modification of the fluid turbulence is seen to be induced by the presence of particles in the bluff-body flow. At first order, the modification of the turbulent properties of the fluid phase are indirectly due to the presence of particles that affect the fluid mean flow. However, by focusing in the jet shear region where fluid/particle correlation can be modelled accurately by using recent theoretical results, we prove that the energy lost by the turbulence in shaking the glass beads is significant when compared to the dominant production term. Moreover, this analysis confirms that the prediction of fluid/particle velocity correlations is a key point for the prediction of turbulence attenuation by partly responsive particles.

As far as the dispersed phase is concerned, we show that the sensitivity to mass loading greatly affects the dispersion of the glass beads. Particles recirculate at the lowest mass loading and the mass concentration of the dispersed phase in the recirculation zone and in the external shear layer is high. This property is interesting for flame stabilization in two-phase combustion. The recirculation at $M_j = 22\%$ is also shown to be efficient to disperse radially the particles in the downstream wake of the bluff-body. On the contrary, the memory of the initial jet is detected far downstream at $M_j = 110\%$, and dispersion of particles is reduced dramatically. Axial or radial profiles of mean and r.m.s. velocity of the dispersed phase are displayed. Relevant Stokes numbers are introduced. The anisotropy of the fluctuating motion of the particles is very large and associated with production mechanisms via interaction with mean velocity gradients. A focus on the jet stagnation region shows that the particulate flow is very sensitive to inertia effects and that no local equilibrium with the fluid turbulence can be assumed when modelling such a configuration.

Finally, even at the small volume ratio considered here, the very high level of turbulent fluctuations typical of the bluff-body flow and the increase of mean mass concentration if the jet stagnates enhance the probability of collisions. A recent application of the kinetic theory to a binary mixture of particles applied to the polydispersed situation shows that collisions are very probable all along the inner jet flow at the highest mass loading. One result of the present experiment conducted at two different mass loadings of glass beads is thus that for increasing but moderate mass loading, the region of the particulate flow concerned with collisions will occupy an increasing domain upstream of the mean stagnation region before affecting the whole jet region.

The data and analysis presented provide a severe test case for the recent development in two-phase flow modelling. These models are more and more sophisticated in order to take into account correctly two-way coupling and collision effects in poly-dispersed particle laden flows. We have shown that such performances are necessary in the present situation if we want to predict and optimize the dispersion and eventually the combustion of particles in practical devices over a wide range of working parameters.

This situation also offers further challenges both to experimentation and modelling. The large-scale intermittency characteristic of the recirculation zone has been discussed in this paper and in a large number of references. As statistical modelling is involved, accurate models of fluid/particle correlated motion are essential. A challenge for the experimentalist is to evaluate the associated correlations. On the other hand, the role of the instantaneous spatial distribution of the dispersed phase in the large-scale recirculation is very important when combustion (of isolated or groups of particles) and therefore pollutant formation takes place. This flow is therefore a good candidate to test recent prediction tools based on large-eddy simulation. Experimental data are then needed to emphasize the spatial structure of the flow and the associated dynamical behaviour of the dispersed phase. Particle image velocimetry is applied in this context in an ongoing work.

Appendix A. Parameters of the PDA system

Transmitting Optics
Colours of the beams: green for U velocity/blue for V velocity

Gaussian beam diameter	1.4 mm
Focal length of the front lens	600 mm
Beam separation	38 mm
Diameter of the measurement volume	G: 281 µm/B: 266 µm
Length of the measurement volume	G: 8.9 mm/B: 8.4 mm
Fringe number	35
Fringe spacing	G: 8.1 µm/B: 7.7 µm
Shift frequency	40 MHz

Receiving Optics

Off-axis angle	$-64°$
Front lens focal length	310 mm
Diameter range	0–155 µm
Phase factors	U1_2: $-3.3524°/$ µm
	U1_3: $-1.6762°/$ µm
Width of the slit	100 µm
Magnification of receiving optics	2
Effective length of the measurement volume	200 µm

Appendix B. Computation of the corrected mass fluxes and mass concentration per size classes from the PDA data at the jet exit

B.1. *Determination of the quantities for the particle class $d_p \in [d_{pi}, d_{pi} + \delta d]$ and velocity class $U \in [U_{ik}, U_{ik} + \delta u]$*

During the measurement time t_m, for the size class i and the velocity class k, the following simple relations hold for (i) $C_{mik}(\mathrm{kg\,m^{-3}})$, the mean mass concentration of particles per unit volume; (ii) $C_{ik}(\mathrm{m^{-3}})$ the mean number concentration of particles per unit volume, and (iii) $f_{mik}^{(n)}(\mathrm{kg\,m^{-2}\,s^{-1}})$ the mean mass flux of particles in direction (n):

$$t_m \| U_{ik} \| A_{ik} C_{ik} = N_{ik} = N_{ik}^d / \eta_{ik}, \tag{B 1}$$

$$t_m \| U_{ik} \| A_{ik} C_{mik} = m_i N_{ik} = m_i N_{ik}^d / \eta_{ik}, \tag{B 2}$$

$$f_{mik}^{(n)} = C_{mik}(U_{ik} \cdot n), \tag{B 3}$$

m_i is the mass of particles of class i. A_{ik} is the surface of the measurement volume seen by particles of diameter class i and velocity class k. N_{ik} is the total number of particles of diameter class i and velocity class k flowing through the measurement surface during t_m. N_{ik}^d is the total number of particles of diameter class i and velocity class k detected by PDA during t_m. η_{ik} is the ratio between N_{ik}^d and N_{ik}, i.e. $\eta_{ik} \in [0, 1]$. This ratio takes into account the occurrence of non-validated samples.

Therefore,

$$C_{ik} = \frac{N_{ik}^d}{\eta_{ik} t_m \| U_{ik} \| A_{ik}} = \frac{1}{\eta_{ik} A_{ik}} \sum_{j=1}^{N_{ik}^d} \frac{1}{\| U_{ikj} \| t_m}, \tag{B 4}$$

$$C_{mik} = \frac{m_i N_{ik}^d}{\eta_{ik} t_m \|\boldsymbol{U}_{ik}\| A_{ik}} = \frac{1}{\eta_{ik} A_{ik}} \sum_{j=1}^{N_{ik}^d} \frac{m_i}{\|\boldsymbol{U}_{ikj}\| t_m}, \tag{B 5}$$

$$f_{mik}^{(n)} = C_{mik}(\boldsymbol{U}_{ik} \cdot \boldsymbol{n}) = \frac{1}{\eta_{ik} A_{ik}} \sum_{j=1}^{N_{ik}^d} \frac{m_i(\boldsymbol{U}_{ikj} \cdot \boldsymbol{n})}{\|\boldsymbol{U}_{ikj}\| t_m}. \tag{B 6}$$

At the exit of the tube in the present study or more generally in quasi-parallel turbulent flows of moderate turbulent intensity, one velocity class is considered and these relations are classically simplified with $\|\boldsymbol{U}_{i1j}\| \approx \langle U_1 \rangle_{pi}$ (direction (1) is the longitudinal direction) to obtain:

$$f_{mi}^{(1)} = \frac{1}{\eta_i A_i} \left(\frac{m_i N_i^d}{t_m} \right) = C_{mi} \langle U_1 \rangle_{pi}. \tag{B 7}$$

This statement is not true in complex three-dimensional flows of high turbulence intensity. A summation over the velocity space is then necessary with:

$$C_i = \sum_k \left(\frac{1}{\eta_{ik} A_{ik}} \sum_{j=1}^{N_{ik}^d} \frac{1}{\|\boldsymbol{U}_{ikj}\| t_m} \right), \tag{B 8}$$

$$C_{mi} = \sum_k \left(\frac{1}{\eta_{ik} A_{ik}} \sum_{j=1}^{N_{ik}^d} \frac{m_i}{\|\boldsymbol{U}_{ikj}\| t_m} \right), \tag{B 9}$$

$$f_{mi}^{(n)} = \sum_k \left(\frac{1}{\eta_{ik} A_{ik}} \sum_{j=1}^{N_{ik}^d} \frac{m_i(\boldsymbol{U}_{ikj}\boldsymbol{n})}{\|\boldsymbol{U}_{ikj}\| t_m} \right). \tag{B 10}$$

We stress that the instantaneous value of the velocity modulus and not the mean velocity modulus is used in these relations. The quantities are therefore defined even at the mean stagnation point and in fact very similar to alternative definitions based on the residence time of particles in the measurement volume (Hardalupas & Taylor 1989; Qiu & Sommerfeld 1992). The factor $(1/\eta_{ik} A_{ik})$ is one of the major unknowns for flux or concentration measurements using PDA. The rejection ratio η_{ik} is not known, and eventually varies with the size class. The surface of the measurement volume seen by particles is very strongly dependent on the diameter of the particle class. It depends also to a smaller extent on the direction of the velocity of the incident particle (see Qiu & Sommerfeld 1992 for a review). Starting from equations (B.8)–(B.10) (Sommerfeld & Qiu 1995) have proposed a method in which the maximum amplitude of the Doppler burst and the integral of the energy of the burst above a given threshold have to be registered by PDA. This method was proved to be reliable even in complex turbulent recirculating flows, but is impossible to apply when commercial systems are used. In the method proposed below, a correction based on the global mass balance of the dispersed phase is adopted. To take into account the strong size dependence of these unknown parameters, the local mass flux is corrected independently for each size class for varying size of the measurement surface seen by the receiving optics and for rejected data. The directional dependence of η_{ik} and A_{ik} is not taken into account. It should, however, be a correction of second order when compared to the particle size dependence correction.

Equations (B.7)–(B.9) then become (N being the total number of detected particles):

$$C_i = \frac{1}{\eta_i A_i} \sum_{j=1}^{N} \frac{1}{\|U_{ij}\| t_m} = \frac{C_i^*}{\eta_i A_i}, \tag{B 11}$$

$$C_{mi} = \frac{1}{\eta_i A_i} \sum_{j=1}^{N} \frac{m_i}{\|U_{ij}\| t_m} = \frac{C_{mi}^*}{\eta_i A_i}, \tag{B 12}$$

$$f_{mi}^{(n)} = \frac{1}{\eta_i A_i} \sum_{j=1}^{N} \frac{m_i(U_{ij} \cdot n)}{\|U_{ij}\| t_m} = \frac{f_{mi}^{*(n)}}{\eta_i A_i}. \tag{B 13}$$

Quantities C_i^*, C_{mi}^* and $f_{mi}^{*(n)}$ are first computed from the data. In determining the modulus of the velocity $\|U_{ij}\| = \sqrt{U_{ij}^2 + V_{ij}^2 + W_{ij}^2}$, only two components are known from the two-component PDA measurements. The unknown W_{ij} has zero mean value. Assuming further that $w' \approx v'$, an instantaneous value of W_{ij} is determined by a random number generator having a Gaussian p.d.f. and an r.m.s. $w' = v'$.

$\dot{M}_i(\text{kg s}^{-1})$ is the total mass per second of particles of class i flowing along the set-up which is known for a given experiment. It is related to the local mass flux by:

$$\dot{M}_i = \int_0^{R_2} f_{mi}^{(1)} 2\pi r \mathrm{d}r, \tag{B 14}$$

where (1) is the longitudinal direction. We suppose now that both the ratio of rejected particles and the measurement surface are constant all across the profile. This hypothesis is valid when the global mass loading is low, which is true in most of the bluff-body flow. It can be very crude in dense particle-laden flows as more and more particles intercept the beams as we move across the profile. Measurements discussed in this work show that this assumption provides a good evaluation.

Using (B.12), we obtain:

$$\dot{M}_i = \frac{1}{\eta_i A_i} \int_0^{R_2} f_{mi}^{*(1)} 2\pi r \mathrm{d}r. \tag{B 15}$$

The value of the product $\eta_i A_i$ that satisfies the global mass conservation equation is thus computed from the measurements and used in relations (B.11), (B.12) and (B.13) in order to obtain the local concentration and mass fluxes. The relative error on the local values of these quantities can be estimated and is of order $E \approx 10\%$.

REFERENCES

ABBAS, T., COSTEN, P. & LOCKWOOD, F. C. 1991 The influence of near burner region aerodynamics on the formation and emission of nitrogen oxides in a pulverized coal furnace. *Combust. Flame* **91**, 346–363.

ABRAHAMSON, A. J. 1975 Collision rates of small particles in a vigorously turbulent fluid. *Chem. Eng. Sci.* **30**: 1371–1379.

ANDERSON, S. L. & LONGMIRE, E. K. 1995 Particle motion in the stagnation zone of an impinging air jet. *J. Fluid Mech.* **299**, 333–366.

BERLEMONT, A., DESJONQUERES, P. & GOUESBET, G. 1990 Particle Lagrangian simulation in turbulent flows. *Intl J. Multiphase Flow* **16**, 19–34.

BERLEMONT, A., SIMONIN, O. & SOMMERFELD, M. 1995 Validation of inter-particle collision models based on large eddy simulation. *Proc. ASME. Symp. on Gas Solid Flows*, vol. 228, pp. 359–369.

BOIVIN, M., SIMONIN, O. & SQUIRE, K. D. 1998 Direct numerical simulation of turbulence modulation by particles in isotropic turbulence. *J. Fluid Mech.* **375**, 235–263.

CARAMAN, N., BORÉE, J., ISHIMA, T. & SIMONIN, O. 2001 Measurements of particle response to turbulence structure in a fully developed pipe flow. *ICMF 2001* (ed. E. E. Michaelides), New Orleans, 27 May–1 June.

CHEN, R. H., DRISCOLL, J. F., KELLY, J., NAMAZIAN, M. & SCHEFFER, R. W. 1990 A comparison of bluff-body and swirl-stabilized flames. *Combust. Sci. Tech.* **71**, 197–217.

CHIN, P. C. & TANKIN, R. S. 1992 Vortical structures from a two-dimensional nozzle with a bluff-body slot. *Phys. Fluids* A **4**, 1724–1736.

COMTE-BELLOT, G. 1965 Ecoulement turbulent entre deux parois parallèles. Publications Scientifiques et Techniques du Ministère de l'air.

CROWE, C. 2000 On models for turbulence modulation in fluid–particle flows. *Intl J. Multiphase Flow* **26**, 719–727.

CROWE, C., SOMMERFELD, M. & TSUJI, Y. 1998 Multiphase Flows with Droplets and Particles. CRC Press.

ELGOBASHI, S. E. & ABOU-ARAB, T. W. 1983 A two-equation turbulence model for two-phase flows. *Phys. Fluids* **26**, 931–938.

FESSLER, J. R. & EATON, J. K. 1999 Turbulence modification by particles in a backward-facing step flow. *J. Fluid Mech.* **394**, 97–117.

FESSLER, J. R., KULICK, J. D. & EATON, J. K. 1994 Preferential concentration of particles in a turbulent channel flow. *Phys. Fluids* **6**, 3742–3749.

FEVRIER, P. & SIMONIN, O. 1998 Constitutive relations for fluid–particle velocity correlations in gas–solid turbulent flows. *Third Intl Conf. on Multiphase Flows, ICMF'98* (ed. J. Batuille), Lyon, 8–12 June.

GOURDEL, C., SIMONIN, O. & BRUNIER, E. 1998 Modelling and simulation of gas–solid turbulent flows with a binary mixture of particles. *Third Intl Conf. on Multiphase Flows, ICMF'98* (ed. J. Batuille), Lyon, 8–12 June.

GOURDEL, C., SIMONIN, O. & BRUNIER, E. 1999 Two-Maxwellian equilibrium distribution function for the modelling of a binary mixture of particles. *Circulating Fluidized Bed Technology VI* (ed. J. Werther), pp. 205–210. Frankfurt am Main, Germany. Dechema.

HARDALUPAS, Y., LIU, C. H. & WHITELAW, J. H. 1994 Experiments with disk stabilised kerosene-fuelled flames. *Combust. Sci. Tech.* **97**, 157–191.

HARDALUPAS, Y. & TAYLOR, A. K. M. P. 1989 On the measurement of particle concentration near a stagnation point. *Exps. Fluids* **8**, 113–118.

HARDALUPAS, Y., TAYLOR, A. K. M. P. & WHITELAW, J. H. 1989 Velocity and particle-flux characteristics of turbulent particle-laden jets. *Proc. R. Soc. Lond.* A **426**, 31–78.

HARDALUPAS, Y., TAYLOR, A. K. M. P. & WHITELAW, J. H. 1992 Particle dispersion in a vertical round sudden-expansion flow. *Proc. R. Soc. Lond.* A **341**, 411–442.

HINZE, J. O. 1975 *Turbulence*. McGraw-Hill.

HISHIDA, K., ANDO, A. & MAEDA, M. 1992 Experiments on particle dispersion in a turbulent mixing layer. *Intl J. Multiphase Flow* **18**, 181–194.

HISHIDA, K. & SATO, Y. 1998 Turbulence structure of dispersed two-phase flows (measurements by laser techniques and modelling). *Third Intl Conf. on Multiphase Flows, ICMF'98* (ed. J. Batuille), Lyon, 8–12 June.

ISHIMA, T., BORÉE, J., FANOUILLÈRE, P. & FLOUR, I. 1999 Presentation of a data base obtained in a confined bluff body flow laden with polydispersed solid particles. Ninth workshop on Two Phase Flow Predictions, http://www-mvt.iw.uni-halle.de/mvt-home.html, Merseburg, 13–16 April.

ISHIMA, T., BORÉE, J., FANOUILLÈRE, P. & FLOUR, I. 2000 Experimental analysis of a confined bluff body flow laden with polydispersed solid particles. Selected Papers of *Ninth Intl Symp. on Applications of Laser Techniques to Fluid Mechanics* (ed. R. J. Adrian, D. Dunao, M. Heiton, M. Maeda, C. Tropea & J. H. Whitelaw).

ISHIMA, T., HISHIDA, K. & MAEDA, M. 1993 Effects of particle residence time on particle dispersion in a plane mixing layer. *Trans. ASME: J. Fluids Engng* **115**, 751–759.

KULICK, J. D., FESSLER, J. R. & EATON, J. K. 1994 Particle response and turbulence modification in fully developed channel flow. *J. Fluid Mech.* **277**, 109–134.

LAVIEVILLE, J. 1997 Simulation numérique et modélisation des interactions entre l'entrainement par la turbulence et les collisions interparticulaires en écoulements gaz–solides. Thèse de l'université de Rouen.

LAVIEVILLE, J., SIMONIN, O., BERLEMONT, A. & CHANG, Z. 1997 Validation of inter-particle collision models based on large eddy simulation in gas–solid turbulent homogeneous shear flow. *ASME FEDSM'97*, 22–26 June.

LONGMIRE, E. K., KHALITOV, D. A., ANDERSON, S. L. & BORÉE, J. 1999 Planar field velocity measurements in gas–solid flows. *3rd ASME/JSME Joint Fluid Engineering Conference* (ed. R. J. Adrian), 18–23 July, San Francisco, California.

MAEDA, M., HISHIDA, K. & FURUTANI, T. 1980 Optical measurements of local gas and particles velocity in an upward flowing dilute gas–solids suspension. *Proc. Polyphase Flow and Transport Technology*. Century 2-ETC, San Francisco.

MODARESS, D., TAN, H. & ELGOBASHI, S. E. 1984 Two-component LDA measurement in a two-phase turbulent jet. *AIAA J.* **22**, 624–630.

NAMAZIAN, M., KELLY, J. & SCHEFFER, R. W. 1992 Concentration imaging measurements in turbulent concentric-jet flows. *AIAA J.* **30**, 384–394.

PERRIN, M., NAMAZIAN, M., KELLY, J. & SCHEFFER, R. W. 1990 Effect of confinement and blockage ratio on nonpremixed turbulent bluff-body burner flames. *23rd Intl Symp. on Combustion, Orleans, France*. The Combustion Institute, Pittsburgh.

PRÉVOST, F., BORÉE, J., NUGLISCH, H. J. & CHARNAY, G. 1996 Measurements of fluid/particle correlated motion in the far field of an axisymmetric jet. *Intl J. Multiphase Flow* **22**, 685–703.

QIU, H. H. & SOMMERFELD, M. 1992 A reliable method for determining the measurement volume size and particle mass fluxes using phase-Doppler anemometry. *Exps Fluids* **13**, 393–404.

ROGERS, C. B. & EATON, J. K. 1991 The effect of small particles on fluid turbulence in a flat-plate, turbulent boundary layer in air. *Phys. Fluids* A **35**, 928–937.

SCHEFFER, R. W., KELLY, J. & NAMAZIAN, M. 1987 Velocity measurements in a turbulent nonpremixed bluff-body stabilized flames. *Combust. Sci. Tech.* **56**, 101–138.

SCHEFFER, R. W., NAMAZIAN, M. & KELLY, J. 1994 Velocity measurements in turbulent bluff-body stabilized flows. *AIAA J.* **32**, 1844–1851.

SIMONIN, O. 1991 Prediction of the dispersed phase turbulence in particle-laden jets. *Proc. 4th Intl Symp. on Gas Solid Flows*. ASME FED, vol. 121, pp. 197–206.

SIMONIN, O., DEUTCH, E. & BOIVIN, M. 1995 Large eddy simulation and second moment closure model of particle fluctuating motion in two-phase turbulent shear flows. *Selected Papers from the Ninth Intl Symp. on Turbulent Shear Flows* (ed. F. Durst, N. Kasagi, B. E. Launder, F. W. Schmidt, K. Suzuki, J. H. Whitelaw). Springer.

SNYDER, W. H. & LUMLEY, J. L. 1971 Some measurements of particle velocity autocorrelation functions in a turbulent flow. *J. Fluid Mech.* **48**, 41–71.

SOMMERFELD, M. 1993 Review of numerical modelling of dispersed two-phase flows. *Fifth Intl Symp. on Refined Flow Modelling and Turbulence Measurements, Paris*, pp. 901–916. Presses Ponts et Chaussées.

SOMMERFELD, M. 1999 Inter-particle collisions in turbulent flows: a stochastic Lagrangian model. *First Intl Symp. on Turbulence and Shear Flows Phenomena* (ed. S. Banerjee & J. K. Eaton), Santa Barbara, CA, USA.

SOMMERFELD, M. & QIU, H. H. 1995 Particle concentration measurements by phase-Doppler anemometry in complex dispersed two-phase flows. *Exps. Fluids* **18**, 187–198.

SQUIRE, K. D. & EATON, J. K. 1990 Particle response and turbulence modification in isotropic turbulence. *Phys. Fluids* A **2**, 1191–1203.

SQUIRE, K. D. & EATON, J. K. 1994 Effect of selective modification of turbulence on two-equation models for particle-laden turbulent flows. *J. Fluid Engng* **116**, 778–784.

SUNDARAM, S. & COLLINS, L. R. 1997 Collision statistics in an isotropic particle-laden turbulent suspension. Part 1. Direct numerical simulations. *J. Fluid Mech.* **335**, 75–109.

TSUJI, Y., MORIKAWA, Y. & SHIOMI, H. 1984 LDV measurements of an air-solid two-phase flow in a vertical pipe. *J. Fluid Mech.* **139**, 417–434.

VIT, C., FLOUR, I. & SIMONIN, O. 1999 Modelling of a confined bluff body flow laden with poly-dispersed solid particles. *Second Intl Symp. on Two-phase Flow Modelling and Experimentation, Pisa*, 23–26 May.

WANG, Q. & SQUIRE, K. D. 1996 Large eddy simulation of particle-laden turbulent channel flow. *Phys. Fluids* A **8**, 1207–1223.

WELLS, M. R. & STOCK, D. E. 1983 The effects of crossing trajectories on the dispersion of particles in a turbulent flow. *J. Fluid Mech.* **136**, 31–62.